Article

Glutamate gating of AMPA-subtype iGluRs at physiological temperatures

https://doi.org/10.1038/s41586-025-08770-0

Received: 5 September 2024

Accepted: 11 February 2025

Published online: 26 March 2025

Open access

Check for updates

Anish Kumar Mondal[1,2], Elisa Carrillo[3], Vasanthi Jayaraman[3,4] ✉ & Edward C. Twomey[1,2,5,6] ✉

Ionotropic glutamate receptors (iGluRs) are tetrameric ligand-gated ion channels that mediate most excitatory neurotransmission[1]. iGluRs are gated by glutamate, where on glutamate binding, they open their ion channels to enable cation influx into postsynaptic neurons, initiating signal transduction[1,2]. The structural mechanics of how glutamate gating occurs in full-length iGluRs is not well understood. Here, using the α-amino-3-hydroxy-5-methyl-4-isoxazolepropionic acid subtype iGluR (AMPAR), we identify the glutamate-gating mechanism. AMPAR activation by glutamate is augmented at physiological temperatures. By preparing AMPARs for cryogenic-electron microscopy at these temperatures, we captured the glutamate-gating mechanism. Activation by glutamate initiates ion channel opening that involves all ion channel helices hinging away from the pore axis in a motif that is conserved across all iGluRs. Desensitization occurs when the local dimer pairs decouple and enables closure of the ion channel below through restoring the channel hinges and refolding the channel gate. Our findings define how glutamate gates iGluRs, provide foundations for therapeutic design and demonstrate how physiological temperatures can alter iGluR function.

AMPARs enable cation influx into postsynaptic neurons on the single-millisecond timescale[2]. This fast depolarization is critical for rapid information processing in the brain[3]. AMPAR signalling is tuned throughout the brain by different combinations of AMPAR subunits GluA1–4 in the core tetrameric subunit, and transmembrane AMPAR regulatory proteins (TARPs) that affect AMPAR gating kinetics and synaptic localization[1,3,4]. AMPARs conduct at four subconductance levels (O1–O4) and TARPs augment occupancy of the higher conductance levels[1,5,6].

AMPARs have three main functional states[2]: resting, open and desensitized. AMPARs have an extracellular domain composed of an amino terminal domain (ATD) and ligand binding domain (LBD). Glutamate binding to the LBD initiates the gating cycle, in which AMPARs enter a primed state: the LBD clamshells are closed around the neurotransmitter, but the conformational changes that accommodate activation or desensitization have not yet occurred. Activation of the AMPAR occurs when the LBD dimers couple and pull open the ion channel in the transmembrane domain (TMD) by putting tension on the LBD–TMD linkers, and desensitization occurs when the LBDs, still glutamate bound, relieve tension on the LBD–TMD linkers by LBD dimer decoupling, which closes the ion channel gate.

Because AMPARs activate rapidly, structural studies have required the use of positive allosteric modulators (PAMs) to prevent desensitization. No activated AMPARs have been captured in the presence of only glutamate, nor for any iGluR[1]. What if the glutamate activation mechanism is unique from the activation mechanism in the presence of PAMs?

We proposed that we could use temperature as a tool to capture the glutamate-activated state. Physiological temperatures increase AMPAR ligand affinity[7,8], but may also accelerate AMPAR gating kinetics[9]. We show that AMPAR gating is temperature sensitive, in which both physiological (37 °C) and hyperthermic (42 °C) temperatures augment the activation probability of the receptor. Using this observation, we captured glutamate gating states with cryogenic-electron microscopy (cryo-EM) on samples prepared at 37 and 42 °C. The glutamate-activated state is distinct from the PAM-activated states of AMPARs. During glutamate activation, an activation seal between LBDs holds open the ion channel pore, in which all four ion channel helices hinge away from the pore axis in a mechanism unique from the PAM-activated states. Hinging of the ion channel helices occurs in a twofold symmetric manner in the SYTANLAAF motif, which is conserved in all iGluRs. Desensitization occurs when the LBD activation seal is ruptured, which relaxes the pull on the ion channel helices, closing the pore. Our results provide new foundations for understanding glutamate gating of iGluRs and drug design.

Function at physiological temperatures

To test the idea that AMPAR gating is sensitive to temperature, we used the GluA2–γ2 construct, which mimics synaptic AMPAR function[6,10–13]. GluA2–γ2 is a construct where TARPγ2, an AMPAR auxiliary subunit that promotes channel opening, is fused through its N terminus to the carboxy terminus of GluA2 (modified rat $GluA2_{flip}$, edited to Q at the Q/R site and mutagenized for stability; Methods).

We performed temperature steps (25 to 30 to 37 to 42 °C) and recorded currents from single channels in the presence of 10 mM glutamate (Fig. 1a and Methods). These data generally show that unitary channel currents

[1]Department of Biophysics and Biophysical Chemistry, Johns Hopkins University School of Medicine, Baltimore, MD, USA. [2]Solomon H. Snyder Department of Neuroscience, Johns Hopkins University School of Medicine, Baltimore, MD, USA. [3]Center for Membrane Biology, Department of Biochemistry and Molecular Biology, University of Texas Health Science Center at Houston, Houston, TX, USA. [4]MD Anderson Cancer Center UTHealth Graduate School of Biomedical Sciences, University of Texas Health Science Center at Houston, Houston, TX, USA. [5]The Beckman Center for Cryo-EM at Johns Hopkins, Johns Hopkins University School of Medicine, Baltimore, MD, USA. [6]Diana Helis Henry Medical Research Foundation, New Orleans, LA, USA. ✉e-mail: Vasanthi.Jayaraman@uth.tmc.edu; Twomey@jhmi.edu

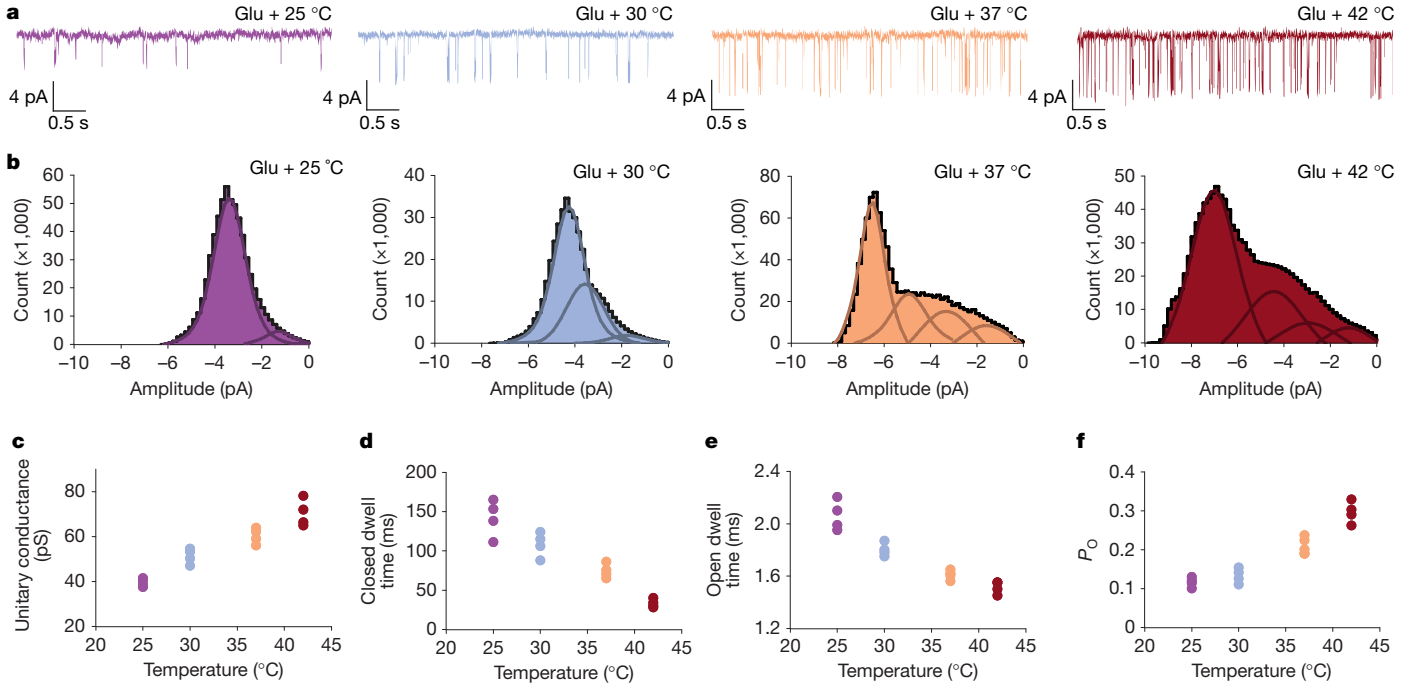

Fig. 1 | Temperature augments AMPAR function. a, Example GluA2–γ2 single channel currents at 25, 30, 37 and 42 °C recorded on a single membrane patch in the presence of 10 mM glutamate (Glu). **b**, Current histograms with Gaussian fits for the amplitude events. Four conductance levels (12, 35, 45 and 65 pS) were observed. **c**–**f**, Average unitary conductance (**c**), average closed dwell time (**d**), open dwell time (**e**) and channel open probability (P_O) (**f**) for single channel membrane patches at each temperature ($n = 4$ patch current recordings for each of 25, 30, 37 and 42 °C). The amplitude events were recorded for 1–2 min at each temperature step per patch. The total times recorded for each temperature step were: 8 min (25 °C), 5 min (30 °C), 7 min (37 °C) and 5 min (42 °C). The *P* value between 25 and 42 °C is less than or equal to 0.0001 for all observables shown in **c**–**f**. *P* value was determined using a two-sided *t*-test.

activated by glutamate are more frequent and larger when temperature is increased (Fig 1a). This also occurs in wild-type GluA2 and GluA2 coexpressed with γ2; as expected, the effects are more pronounced in the presence of γ2, which enhances AMPAR activation (Extended Data Fig. 1a,b), and the effects are AMPAR-dependent (Extended Data Fig. 1c). AMPARs conduct to many subconductance levels, whereas GluA2–γ2 complexes show four subconductance levels (O1–O4)[5,6]. Idealization of the single channel recordings reveal occupancy of O1–O4 is temperature dependent (Fig. 1b). The subconductance levels we observe are O1 (roughly 12 pS), O2 (roughly 35 pS), O3 (roughly 45 pS) and O4 (roughly 65 pS). At room temperature (25 °C), the current histogram is best fitted with two Gaussian components, corresponding to two conductance levels, the mean amplitudes (and populations) of which are 12 ± 1.7 pS (5 ± 0.4%) and 35 ± 5.2 pS (90 ± 5%). At 30 °C, the current histogram and Gaussian fitting reveals three conductance levels: 12 ± 1.1 pS (4.5 ± 0.5%), 35 ± 0.9 pS (8 ± 0.6%) and 45 ± 4.8 pS (84 ± 4.5%). Stepping to physiological temperature (37 °C) further augments channel subconductance, in which four conductance levels are observed: 12 ± 1.3 pS (4.5 ± 0.6%), 35 ± 3.7 pS (10 ± 1.2%), 45 ± 5.1 pS (14 ± 1.6%) and 65 ± 2.4 pS (62 ± 6.1%). Channels at hyperthermic temperature (42 °C) have increased occupancies of the higher conductance levels, which is exemplified by 72 ± 7% occupancy of the highest subconductance level, O4. The overall changes in channel subconductance are reflected in the mean unitary channel conductance, in which the mean conductances are roughly 40 pS at 25 °C, 50 pS at 30 °C, 60 pS at 37 °C and 70 pS at 42 °C (Fig. 1c).

The 25 °C unitary conductance is in line with previous single channel recordings performed on single AMPAR–TARP complexes at room temperature[6,14–16]. Physiological temperature (37 °C) markedly increases the average conductance, with hyperthermic temperature (42 °C) showing a roughly 1.75 times increase in unitary conductance compared to room temperature with a temperature coefficient (Q_{10}) of 1.3. However, inversely, both the mean shut and open dwell times decrease as temperature increases (Fig. 1d,e). The mean shut time decreases from 138.2 ± 27 ms at 25 °C by a factor of four to 34 ± 6 ms at 42 °C with a Q_{10} of 2.5 (Fig. 1d). The mean open channel dwell time decreases by a factor of roughly 1.4 from 25 °C (2.06 ± 0.05 ms) to 42 °C (1.5 ± 0.02 ms) with a Q_{10} of 1.2 (Fig. 1e). Thus, although both the mean shut and open dwell times are decreased, temperature has a more marked effect on reducing the channel shut time, which may be reflective of increased agonist binding affinity at physiological temperatures[7].

The disparate effect on mean channel closed and open times is probably responsible for the change in channel open probability (P_O) as temperature increases (Fig. 1f). At room temperature, the open probability is roughly 8.4%. At 37 °C, this raises to 21.3% and at 42 °C, the P_O raises to 29.6%.

In total, these data indicate that AMPAR gating is augmented at physiological temperatures. Although the relative open dwell time is decreased, unitary channel conductance increases, as does P_O. The increase in channel conductance and decrease in mean open time are consistent with the increase in ion mobility and reaction rates on increasing temperature as predicted by the Arrhenius equation. This is consistent with temperature-dependent gain of function observed in excitatory postsynaptic currents[17], the premise that temperature increases state transitions and ion movements in ion channels[9,18–21], and the prediction that temperature may drive AMPARs into higher subconductance levels[9].

Thus, although AMPARs are not directly temperature gated like some transient receptor potential channels, the channel activation probability by glutamate is sensitive to temperature.

Cryo-EM of glutamate gating

Because physiological temperatures positively influence the gating of GluA2–γ2, we proposed that raising the temperature of GluA2–γ2 during cryo-EM specimen preparation would enable reconstruction of the glutamate-activated state. This also enables us to directly test the idea

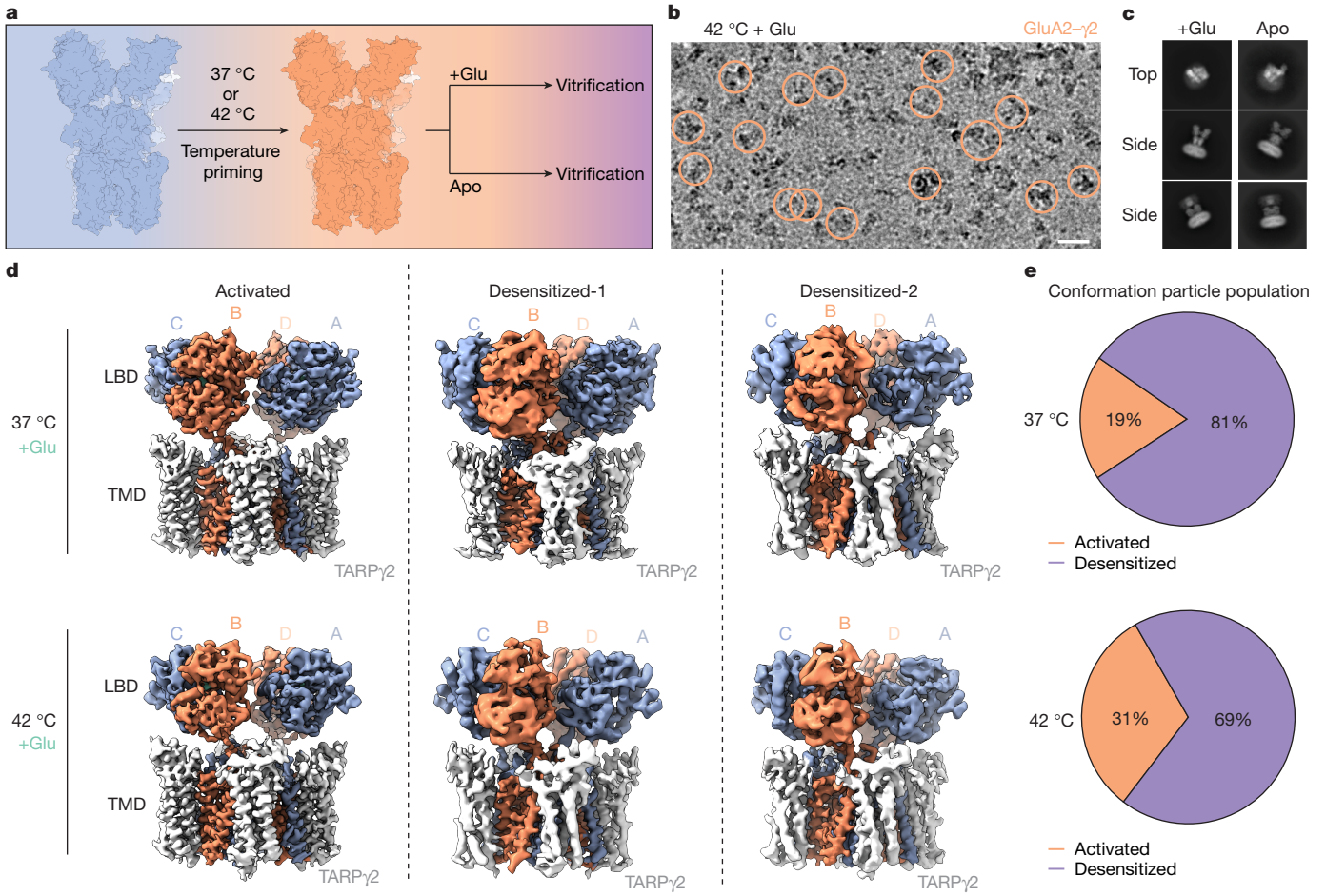

Fig. 2 | Cryo-EM of GluA2–γ2 prepared at physiological temperatures. **a**, Workflow for specimen preparation. **b**, Example micrograph of AMPARs vitrified after priming at 42 °C and 1 mM Glu exposure. **c**, Example 2D classes from 42 °C samples in the presence and absence of Glu. **d**, Gating snapshots from 37 °C (top) and 42 °C (bottom) GluA2–γ2 prepared with glutamate. **e**, Overall particle populations at 37 °C (top) and 42 °C (bottom) that contribute to activated state or desensitized state (desensitized-1 and -2 are combined). Scale bar, 200 Å.

that AMPAR activation is augmented by physiological temperatures through tracking how the cryo-EM particle populations change with temperature. Raising temperatures during cryo-EM specimen preparation has been used to resolve the temperature gating of transient receptor potential channels[22–25], temperature-dependent enzymatic ensembles[26] and temperature-sensitive conformations of other ion channels[27]. We adopt a similar approach here (Methods).

We purified GluA2–γ2 and tested the thermostability of GluA2–γ2 with fluorescence-based size-exclusion chromatography (FSEC) after incubating GluA2–γ2 for 15 minutes at 4, 37 and 42 °C (Extended Data Fig. 2a,b). There was no major difference in the stability of GluA2–γ2 between the temperature incubations as observed by maintenance of the GluA2–γ2 complex peak.

We prepared GluA2–γ2 for cryo-EM using physiological and hyperthermic temperatures (Methods). In brief, GluA2–γ2 was primed for glutamate gating by first incubating the specimen at 37 or 42 °C on a heat block (Fig. 2a). Immediately before vitrification, GluA2–γ2 was spiked with 1 mM glutamate (preheated to 37 or 42 °C) and vitrified using a cryoplunger with the specimen chamber set to 37 or 42 °C. Parallel to this, we prepared GluA2–γ2$_{EM}$ at 42 °C without glutamate to capture the apo or resting state of the receptor (Fig. 2a). The micrographs from GluA2–γ2 prepared at hyperthermic conditions enable definitive identification of single particles (Fig. 2b), and distinct views as revealed by two-dimensional (2D) classification (Fig. 2c).

To parse out the distinct conformational states, we used signal subtraction to remove the AMPAR ATD, focused on the AMPAR LBD and TMD in three-dimensional (3D) classifications and refinements (Methods, Extended Data Figs. 3–5 and Extended Data Tables 1 and 2). This revealed snapshots of one activated state and two desensitized states (desensitized-1 and desensitized-2) from each dataset collected from samples prepared at 37 and 42 °C (Fig. 2d and Extended Data Figs. 3a and 4a). We also collected a control dataset in the absence of glutamate at 42 °C, in which two principle resting states (resting-1, resting-2) were reconstructed (Extended Data Fig. 4b). The resting-1 LBD–TMD was refined to 4.18 Å resolution, with the central TMD reaching 3 Å locally (Extended Data Fig. 5). The resting-2 LBD–TMD was refined to 4.78 Å, with the central TMD reaching 3.5 Å locally (Extended Data Fig. 5).

In the 37 °C dataset, the activated state LBD–TMD was refined to 3.62 Å, and TMD to 3.23 Å (Extended Data Fig. 3). The desesensizited-1 LBD–TMD was refined to 4.17 Å overall, and the LBD–TMD in desensitized-2 to 4.52 Å overall (Extended Data Fig. 3). From the 42 °C dataset, the activated state LBD–TMD was refined to 3.54 Å and TMD to 3.46 Å, (Extended Data Figs. 4a and 5). The desensitized-1 LBD–TMD was refined to 4.48 Å, and the desensitized-2 LBD–TMD was refined to 4.31 Å (Extended Data Figs. 4a and 5).

Each state has four TARPγ2 molecules bound around the AMPAR TMD, as expected. The state of each LBD can be identified, along with AMPAR subunit position, transmembrane (TM) helix, ion channel gate and selectivity filter. The differences between the cryo-EM maps represent different functional states of each class and will be analysed in later parts of this report.

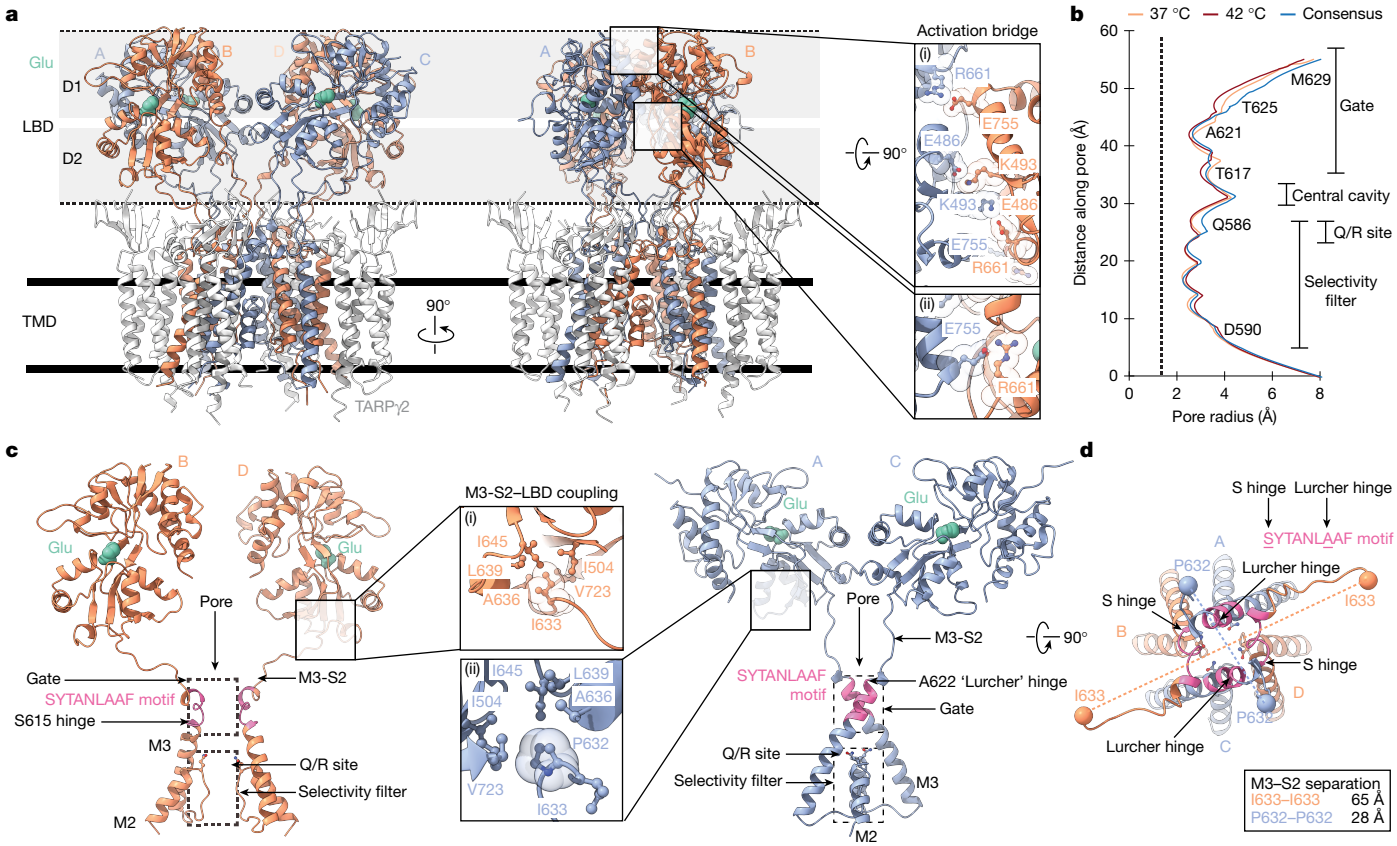

Fig. 3 | Glutamate activation. a, Structure of the GluA2–γ2 glutamate-activated state. Insets (i) and (ii) are close ups of the salt bridges that collectively make the activation bridge. **b**, Pore radius profile (orange) along the ion channel pore for the consensus, 37 and 42 °C activated states. Residues are marked immediately next to the plot, with general features on the right. The dashed line represents the 1.4-Å radius of a water molecule. **c**, Close-up of the symmetric subunit pairs in the glutamate-activated state. B and D subunits (left) and A and C subunits (right). (i) A zoom on the M3-S2–LBD coupling in B and D, and (ii) in A and C. **d**, Top view of the glutamate-activated ion channel pore, rotated 90° from **c** with all four subunits.

Image processing of the cryo-EM data directly demonstrates the effects of temperature on GluA2–γ2 activation probability independent of our single channel data. In our 37 °C dataset, there are 654,059 total particle images that are split across the GluA2–γ2 activated and desensitized states (Extended Data Fig. 3). Overall, 19% of these belong to the activated state, and 81% belong to the desensitized states (Fig. 2e). From image processing of the 42 °C data, 514,951 particle images were split across the states before a final classification improve the map resolutions. This corresponds to an overall split of 31% of the particles corresponding to the activated state, and 69% of the particles corresponding to the desensitized states (Fig. 2e and Extended Data Fig. 4a). The activated particle populations at both 37 and 42 °C approximate the respective P_O values of 21.3 and 29.6% (Fig. 1e).

Thus, cryo-EM not only enabled us to capture snapshots of the glutamate gating states of GluA2–γ2 but also demonstrate that physiological temperatures alter activation probability.

Glutamate activation mechanism

To assess the glutamate activation mechanism, we combined the activated state data to reconstruct a consensus activated map (Extended Data Fig. 6a and Extended Data Table 1). This resolved the consensus activated LBD–TMD to 3.46 Å, and TMD to 3.02 Å (Extended Data Fig. 6b–d). This improved the resolution from each individual activated state and enabled confident modelling of the pore features (Extended Data Fig. 7). Each individual activated state snapshot captured at 37 and 42 °C are near identical, with a root mean squared deviation (r.m.s.d.) of 0.30 Å (Extended Data Fig. 8a–k). This is consistent with temperature affecting activation probability and not a distinct conformational state.

In the activated state, all four LBDs are bound to glutamate, and four molecules of TARPγ2 are bound (Fig. 3a). The receptor is overall twofold symmetric. The LBDs are organized into two local dimers labelled by subunit position (dimer pairs A and D, B and C), of which A and C and B and D are symmetric pairs.

There is marked contact between LBDs in their local dimers, where salt bridges between the LBD upper halves (D1) contact each other extensively (Fig. 3a(i)). Here, the central salt bridges are E486 from (A and C) to K493 (B and D) and K493 (A and C) to E486 (B and D). On the far side of the central salt bridges is a contact between D2 and D1, where R661 (A and C) contacts E755 (B and D) (Fig. 3a(i)). The symmetric pair of this interaction occurs on the outer side of the LBD dimer, where E755 (A and C) is in contact with R661 (B and D) (Fig. 3a(i),(ii)). Collectively, we refer to the group of four salt bridges as the activation bridge. And indeed, the activation bridge is essential for activation: ablating the salt bridges markedly reduces the ability of glutamate to hold the channel open, notably increasing AMPAR desensitization[28,29].

During glutamate binding, the lower D2 half of an LBD swings upward to the D1 half to close around glutamate. Therefore, the R661–E755 salt bridges help to maintain the glutamate-bound state of each LBD by locking the D2 in the glutamate-bound position against its LBD partner.

The activation bridge holds apart the LBD D2s within local LBD dimers. Collectively, this puts tension on the LBD–TMD linkers below (Fig. 3a), which opens the ion channel. As a result, the ion channel is in a putative open state (Fig. 3b). There is minimal variation between the 37 °C, 42 °C and consensus activated state pores (Fig. 3b). The ion

channel gate, at the top of M3 helices, is formed by M629, T625 and T617 is pulled away from the central axis and does not occlude the pore. The minimal constructive radius (r_{min}) at the gate is roughly 2.5 Å. Below, at the selectivity filter, the r_{min} is 2.3 Å. The channel radius at the Q/R site is 2.5 Å. Thus, the pore is expected to be in a conductive state for water and cations such as sodium and calcium.

The open ion channel is held open by the M3-S2 linkers that directly tether the ion channel gate to the LBDs. In the B and D subunit positions, the linkers are held in place by the linker residue I633 being locked into a hydrophobic cavity on the bottom of D2 (Fig. 3c(i)). In the A and C subunit positions, M3-S2 LBD coupling occurs by means of P632 insertion into the hydrophobic cavity (Fig. 3c(ii)). Collectively, this puts tension on the M3-S2 linkers that causes unwinding of each M3 helix in all subunits, opening the ion channel for conductance (Fig. 3d).

The cryo-EM map allows clear identification of the features in the unwound pore helices in the consensus activated map, in addition to the activated maps at 37 and 42 °C (Extended Data Fig. 7). Unwinding of the M3 helices is facilitated by a hinge at S615 in the B and D subunits and A622 in the A and C subunits. In GluA2–γ2 S615 is at the beginning of the SYTANLAAF motif, which is a conserved motif in mammalian iGluRs (Extended Data Fig. 8a–c). A622 is the penultimate residue in the motif. A622 is the site of the 'Lurcher' mutation (A622T) that causes spontaneous activation of iGluRs and leads to excitotoxic cell death[30–34], and has long been of great interest to the field since its discovery in 1997 (ref. 30). Perhaps the Lurcher mutation exacerbates the hinging of the subunits in the A and C subunit positions. Thus, we term the hinging at A622 in the A and C subunits the Lurcher hinge, and the hinging at S615 in the B and D subunits the S hinge.

Whereas hinging in all four M3 helices is unique to this glutamate-activated AMPAR structure, it has been proposed to perhaps be necessary for maximum conductance of the ion channel[6,35]. Furthermore, the twofold symmetric opening of the channel by means of the S hinge and Lurcher hinge agrees with early biochemistry suggesting the that the SYTANLAAF motif imparts a twofold symmetric gate in iGluR ion channels[36].

The SYTANLAAF motif has long been proposed to be critical for iGluR gating[1,37]. Our data show that the entire SYTANLAAF motif is ingrained in gating, and points to why mutations in this motif are so debilitating across the iGluR family[1,38,39].

Glutamate versus PAM activation

To delineate whether glutamate gating is distinct from gating in the presence of PAMs, we compared our glutamate-activated state to a putative PAM-activated state, GluA2–γ2 in the presence of cyclothiazide (CTZ) and glutamate[6,10] (Protein Data Bank (PDB) 5WEO).

Both the activated state and PAM-activated state are twofold symmetric (Fig. 4a,b). In each, all four LBDs are bound to glutamate, but in the PAM-activated state, CTZ is wedged between LBDs (Fig. 4b) to prevent desensitization. The main differences between the states lay within the ion channel.

The ion channel gate is largely similar between the two states (Fig. 4c). The principal difference is at the Q/R site, where the PAM-activated state is notably more constricted to 1.4 versus 2.5 Å in the activated state (Fig. 4c).

In the PAM-activated state, the M3 helices hinge in the B and D subunits at A618, the fourth residue in the SYTANLAAF motif (Fig. 4d). We call this the A hinge. There is no hinging in the A and C subunits in the PAM-activated state, where in the activated state there is a hinge at the Lurcher site (Fig. 4d). This causes an overall shift in the M3 helices (Fig. 4d) that is probably communicated to M2 and the Q/R site through direct connection, thus reflecting the difference in pore radius at the Q/R site.

The landmark residues in the M3-S2 linker (for example, I633 and P632) that help facilitate activation (Fig. 3c) have similar degrees of separation in each state, with the PAM-activated state having marginally greater degrees of separation between I633 in B and D (1 Å) and between P632 in A and C (2 Å; Fig. 4d).

The A hinge in the B and D subunits has been a common feature of all PAM-activated studies that use CTZ[1,2]. Why is there a difference in pore gating between the states? It is well documented that CTZ enhances activation by preventing desensitization[40]. It is possible that the PAM-activated states captured by cryo-EM represent a postactivated state in which the helices have wound back into a relaxed state where the channel is prevented from the conformational transitions that would facilitate desensitization. This idea is consistent with studies suggesting that CTZ does not contribute to activation of AMPARs, but prevents the desensitized state transition[40–42].

An alternative possibility is that the glutamate-activated state captured here is a higher conductance state (O3 or O4) than the PAM-activated state, and kinking at the S and Lurcher hinges is required for occupying the high conductance states. This possibility is consistent with the structural characterization of the low subconductance states of the channel (O1 and O2), in which there are marked differences between the pore profiles of GluA2–γ2 O1 and O2 with the activated state reported here (Fig. 4c). These differences could be due to GluA2–γ2 principally occupying O3 and O4 at 37 and 42 °C (Fig. 1b).

Glutamate-gating mechanism

By isolating gating snapshots and analysing the morphing between modelled structures, we reconstructed and estimated the motion that accompanies AMPAR gating transitions in the context of just glutamate. To estimate the gating transitions, we use the 42 °C data because we collected datasets at 42 °C ± glutamate. In addition to the activated state, we focus on resting-1 and desensitized-2, owing to the data quality (Extended Data Figs. 4, 5 and 7b), and the 42 °C desensitized-1 and -2 states, as well as resting-1 and -2 states, are near identical, with a r.m.s.d. of 0.34 and 0.71 Å, respectively (Extended Data Fig. 8d,e). We focus on the core AMPAR in the centre of the GluA2–γ2 complex to discern the gating mechanism.

The resting (apo) state of the receptor reconstructed at 42 °C is near identical to the resting state GluA2–γ2 incubated at 4 °C before vitrification (1.0 Å r.m.s.d., Extended Data Fig. 8f). Although there are no glutamate-bound GluA2–γ2 desensitized states from cryo-EM outside this study, comparison to desensitized GluA2–γ5 (ref. 43) desensitized states prepared at 4 °C before vitrification shows largely similar LBDs and channel gate (r.m.s.d. 0.92 Å) other than a rotation between the LBD and TMD (r.m.s.d. 5.3 Å), which could be a feature of γ5 (Extended Data Fig. 8g). Our desensitized states resolved from the 37 °C are also near identical (0.36 Å r.m.s.d., Extended Data Fig. 8i), and like the 42 °C desensitized states (r.m.s.d. 0.42 Å, Extended Data Fig. 8j). This is consistent with the gating transitions being temperature sensitive, not direct temperature gating.

The principal differences in the ion channel pore between the gating states are at the Q/R site and the ion channel gate (Fig. 5a). The pore profiles are largely similar between the gating snapshots captured at 37 and 42 °C (Extended Data Fig. 8k). The map quality in each state enables definitive identification of channel features (Extended Data Fig. 7). Although the Q/R site is similar between the resting and activated states, this is constricted on desensitization, perhaps creating a second gate to conductance (Fig. 5a). This is similar to NMDA-subtype iGluRs studied in the absence of PAMs, in which a two gate model was proposed[44,45].

Overlay of each state highlights the gross differences in the LBD that drive gating of the central ion channel, whereas the peripheral transmembrane helices are largely similar (Fig. 5b). At the level of the single LBD, both activated and desensitized states show a 26° difference between D2 and D1 relative to the resting state, which is unbound to glutamate (Fig. 5c).

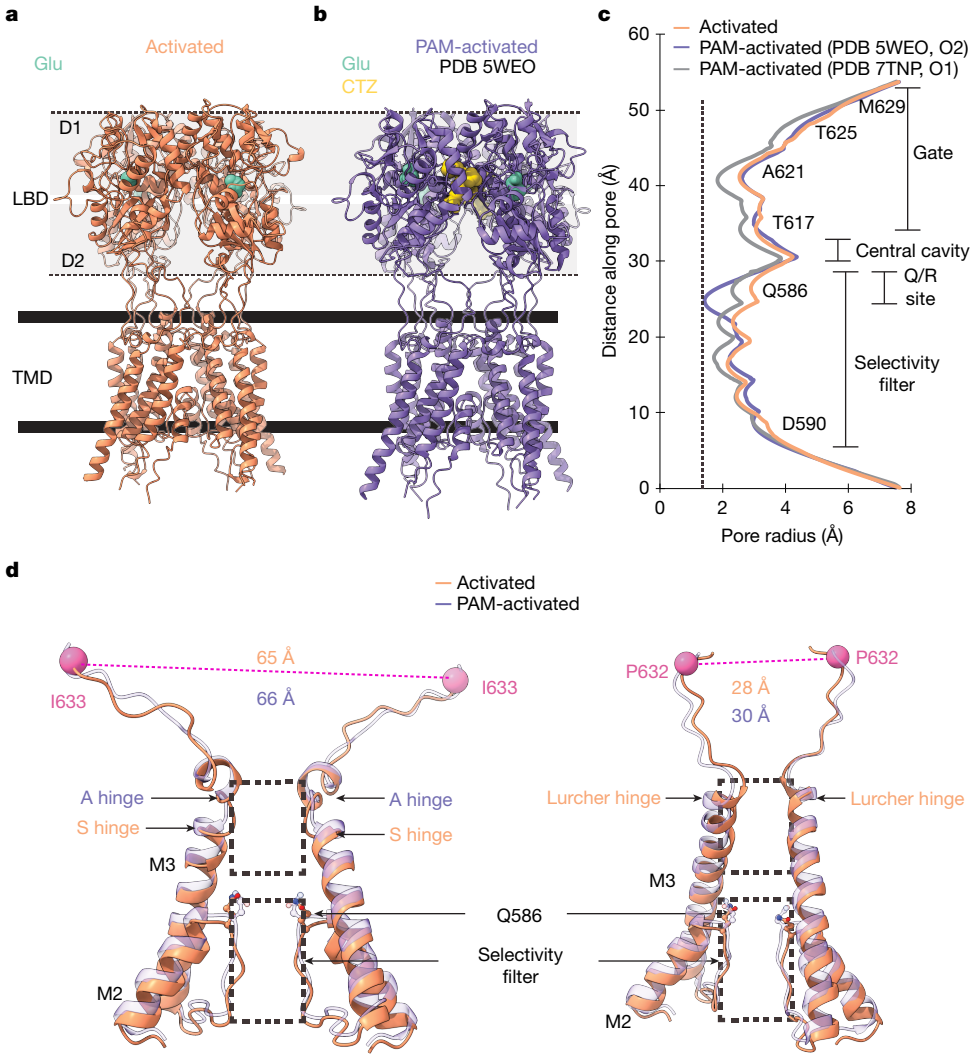

Fig. 4 | Glutamate-activated state compared to a PAM-activated state. **a**, Glutamate-activated state of GluA2–γ2 with γ2 excluded. **b**, PAM-activated state of GluA2–γ2 with γ2 excluded (PDB 5WEO). **c**, Pore radius profile comparison between the activated and both O1 or O2 PAM-activated states. The dashed line represents the 1.4-Å radius of a water molecule. **d**, Comparison between the ion channel pore models of the activated and PAM-activated states. B and D subunits (left) and A and C subunits (right).

Despite the symmetry, the subunit positions are not equivalent in gating of the channel because of the proximity of the LBDs to the pore (Fig. 5d) coupled with the clamshell closure during glutamate binding (Fig. 5c). In the conformational changes associated in the LBD clamshell during glutamate binding, the principal change occurs near the channel pore in the A and C subunits. However, in the B and D subunits, this is distal from the pore. Thus, we consider the A and C subunit LBDs pore proximal, and the B and D subunit LBDs pore distal; as the conformational changes coupled with glutamate gating occur, the motions of the B and D subunits apply greater mechanical torque directly to M3 helices by means of the M3-S2 linkers (below). We propose this is why the B and D subunits cause unwinding further into the SYTANLAAF motif (S hinge) versus the A and C subunits at the Lurcher hinge (Fig. 5d).

Coordinated motion of local dimer pairs is critical to the gating process. At the level of local LBD dimers, there are pairs between the B and C subunits and D and A subunits (Fig. 5e). The relative separation between D2s in the local dimer (measured by S635–S635 distances) versus D1s (measured by S741–S741 distances) is how the tension is applied to the linkers below to open the ion channel. During activation, there is a 9-Å increase in the D2 separation in local dimers, which places tension on the LBD–TMD linkers to open the ion channel. In desensitization, the D2–D2 separation is minimized to 15 Å by maximizing D1–D1 separation by 9 Å in local dimers.

Coordination between local dimers at the tetrameric level dilates the activation ring between LBDs, which enables torque to be applied to the M3 helices below during gating (Fig. 5f). Through comparing our snapshots, we estimate that during activation, the B and D subunits rotate 7° counterclockwise around the gating ring and the A and C subunits rotate 14 °C counterclockwise relative to the resting state. This collective motion dilates the activation ring. The activation ring is compressed in desensitization by 5° clockwise rotation of the B and D subunits, and 36° clockwise rotation of the A and C subunits. This enables relaxation of the channel below back to an inactivated state despite the LBDs being glutamate bound.

The pore-distal and pore-proximal movements of the LBDs have disparate effects on gating. The collective motions of the local LBDs (Fig. 5e) along the tetrameric LBD layer (Fig. 5f) cause the pore-distal B and D LBDs separate to 63 Å during activation (S635 B to S635 D), which unwinds the M3 helices to the beginning of the SYTANLAAF motif at S615 (Fig. 5g). Distance-wise, the pore-proximal LBDs get 5 Å closer (S635 A to S635 C). However, the torque applied by the conformational change of the LBDs causes unwinding to the Lurcher hinge. As the LBDs rotate back during desensitization (Fig. 5f), the helices are wound back

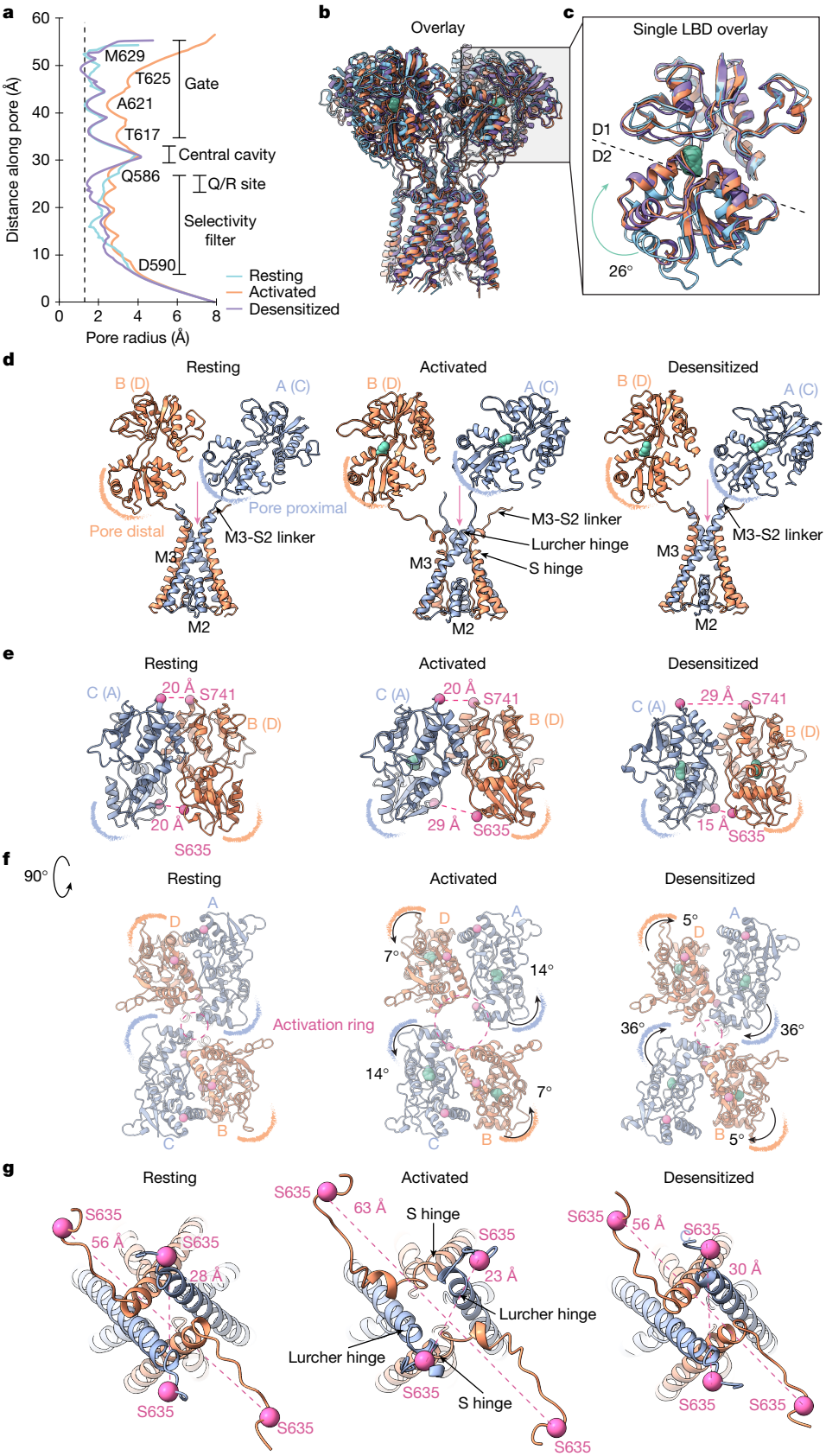

Fig. 5 | Structural mechanism of glutamate gating. a, Pore radius profiles in each gating state snapshot. Dashed line represents the 1.4-Å radius of a water molecule. **b**, Overlay of each state, aligned by means of the TMD. **c**, Alignment of a single LBD from each state defines the conformational change associated with glutamate binding. **d**, Opposite LBD pairs (B and A; D and C omitted for clarity) with the ion channel pore below (all subunits) to show the non-equivalent LBD subunit positions. **e**, Local LBD dimer pairs with their D1–D1 and D2–D2 distance marker residues in each gating state. **f**, LBD tetramers viewed from the top (90° rotated from **e**) in each gating state. The activation ring between the LBDs dilates during activation. **g**, Top view of the ion channel immediately below the LBD tetramer in each gating state. The D2 residue S635 is shown to illustrate the relative positioning of each LBD D2 relative to the central ion channel pore.

and the gate is restored. Like the hinging of all four M3 helices causing pore dilation at the Q/R site, desensitization appears to narrow the Q/R site to less than 1.4 Å (Fig. 5a). Given the notable changes observed at the gate and Q/R site, it is possible that changes at both sites contribute to subconductance[6] and mutagenesis at the Q/R site effects channel conductance[1,16,46,47].

Discussion

AMPARs, when binding glutamate, transition to other conformational states through a pre-active intermediate[2] (Extended Data Fig. 2c). Activation is accommodated by D1–D1 contacts between LBDs, an action puts tension on the M3-S2 linkers and opens the channel by means of the S hinge (B and D subunits) and the Lurcher hinge (A and C subunits). During desensitization, the LBDs remain glutamate bound, but D2–D2 contacts between LBDs enable relaxation of the tension on M3-S2 linkers, enabling closure of the upper gate, and a finer constriction at the Q/R site. Activation in the presence of a PAM, such as CTZ, captures activated channels where the channel is held open by the A hinge in the B and D subunits (Extended Data Fig. 2c). Negative allosteric modulators such as perampanel and GYKI-52466 bind in the ion channel collar and prevent hinging of the M3 helices, pushing the receptors into an inhibited, desensitized-like state[13,48] (Extended Data Fig. 2c).

Supporting the possibility of the Q/R site being a second gate are recent cryo-EM studies on iGluRs. Kainate-subtype iGluRs show dynamic changes at their upper gate as well as their Q/R site equivalent[35]. Furthermore, in AMPAR structures where the upper gate is open (for example, greater than or equal to 2.0 Å), only lower conductance levels are observed, potentially because the channel was restricted at the Q/R site[6]. This is highlighted by comparison of the PAM-activated pore to the glutamate-activated pore, where there is a 1.1-Å greater constriction at the Q/R site (Fig. 4c). It is possible that dilation of the Q/R site contributes to channel subconductance through functioning as a lower gate.

AMPAR gating is augmented at physiological temperatures, which underscores the importance of regulating proper brain temperature, and in considering temperature when studying iGluR function. Our results indicate that augmentation of receptor activation is principally driven by the reduction of the closed channel dwell time as temperature increases. Thus, the receptors activate more frequently, akin to a combustion engine increasing its revolutions per minute to initiate combustion.

The glutamate-activated channel hinges in all four pore helices and involves the entirety of the SYTANLAAF motif that is conserved in iGluRs[1,35,49] (Extended Data Fig. 8a). The involvement of the entire SYTANLAAF motif in gating by means of the S hinge and Lurcher hinge in our glutamate-activated states is unique from pore opening mechanisms in all iGluR structures with PAMs present (Extended Data Fig. 8b,c).

Several critical questions remain. For example, native AMPARs are distinct from the GluA2–γ2 cryo-EM construct used here, have unique GluA subunit compositions, and auxiliary subunit binding partners[50]. Although the native overall topology is identical to GluA2–γ2, the mechanisms of how the native compositions alter temperature sensitivity and activation probability are unknown. For example, in native AMPARs, the ATD layer is highly flexible and dynamic[50]. The properties of the ATD require further exploration in glutamate gating, considering its sensitivity to pH and unique properties in GluA subunits[51,52]. Furthermore, AMPARs show modal gating behaviours, in which the receptors gate in both low and high open probability modes[1,53,54]. What dictates the modal behaviour is still unclear.

The insights from this study will open new avenues for considering temperature in iGluR gating, therapeutic design, and using temperature-resolved cryo-EM to capture states of proteins that are more highly populated at physiological temperatures.

Online content

Any methods, additional references, Nature Portfolio reporting summaries, source data, extended data, supplementary information, acknowledgements, peer review information; details of author contributions and competing interests; and statements of data and code availability are available at https://doi.org/10.1038/s41586-025-08770-0.

1. Hansen, K. B. et al. Structure, function, and pharmacology of glutamate receptor ion channels. *Pharmacol. Rev.* **73**, 298–487 (2021).
2. Twomey, E. C. & Sobolevsky, A. I. Structural mechanisms of gating in ionotropic glutamate receptors. *Biochemistry* **57**, 267–276 (2018).
3. Diering, G. H. & Huganir, R. L. The AMPA receptor code of synaptic plasticity. *Neuron* **100**, 314–329 (2018).
4. Twomey, E. C., Yelshanskaya, M. V. & Sobolevsky, A. I. Structural and functional insights into transmembrane AMPA receptor regulatory protein complexes. *J. Gen. Physiol.* **151**, 1347–1356 (2019).
5. Tomita, S. et al. Stargazin modulates AMPA receptor gating and trafficking by distinct domains. *Nature* **435**, 1052–1058 (2005).
6. Yelshanskaya, M. V., Patel, D. S., Kottke, C. M., Kurnikova, M. G. & Sobolevsky, A. I. Opening of glutamate receptor channel to subconductance levels. *Nature* **605**, 172–178 (2022).
7. Shahi, K. & Baudry, M. Increasing binding affinity of agonists to glutamate receptors increases synaptic responses at glutamatergic synapses. *Proc. Natl Acad. Sci. USA* **89**, 6881–6885 (1992).
8. Tocco, G., Massicotte, G., Standley, S., Thompson, R. F. & Baudry, M. Effect of temperature and calcium on the binding properties of the AMPA receptor in frozen rat brain sections. *Eur. J. Neurosci.* **4**, 1093–1103 (1992).
9. Postlethwaite, M., Hennig, M. H., Steinert, J. R., Graham, B. P. & Forsythe, I. D. Acceleration of AMPA receptor kinetics underlies temperature-dependent changes in synaptic strength at the rat calyx of Held. *J. Physiol.* **579**, 69–84 (2007).
10. Twomey, E. C., Yelshanskaya, M. V., Grassucci, R. A., Frank, J. & Sobolevsky, A. I. Channel opening and gating mechanism in AMPA-subtype glutamate receptors. *Nature* **549**, 60–65 (2017).
11. Twomey, E. C., Yelshanskaya, M. V., Vassilevski, A. A. & Sobolevsky, A. I. Mechanisms of channel block in calcium-permeable AMPA receptors. *Neuron* **99**, 956–968.e4 (2018).
12. Twomey, E. C., Yelshanskaya, M. V., Grassucci, R. A., Frank, J. & Sobolevsky, A. I. Elucidation of AMPA receptor-stargazin complexes by cryo-electron microscopy. *Science* **353**, 83–86 (2016).
13. Hale, W. D. et al. Allosteric competition and inhibition in AMPA receptors. *Nat. Struct. Mol. Biol.* https://doi.org/10.1038/s41594-024-01328-0 (2024).
14. Shelley, C., Farrant, M. & Cull-Candy, S. G. TARP-associated AMPA receptors display an increased maximum channel conductance and multiple kinetically distinct open states. *J. Physiol.* **590**, 5723–5738 (2012).
15. Zhang, W. et al. Unitary properties of AMPA receptors with reduced desensitization. *Biophys. J.* **113**, 2218–2235 (2017).
16. Carrillo, E., Bhatia, N. K., Akimzhanov, A. M. & Jayaraman, V. Activity dependent inhibition of AMPA receptors by Zn^{2+}. *J. Neurosci.* **40**, 8629–8636 (2020).
17. Korinek, M., Sedlacek, M., Cais, O., Dittert, I. & Vyklicky, L. Temperature dependence of *N*-methyl-D-aspartate receptor channels and *N*-methyl-D-aspartate receptor excitatory postsynaptic currents. *Neuroscience* **165**, 736–748 (2010).
18. Milburn, T., Saint, D. A. & Chung, S. H. The temperature dependence of conductance of the sodium channel: implications for mechanisms of ion permeation. *Recept. Channels* **3**, 201–211 (1995).
19. Hoffmann, H. M. & Dionne, V. E. Temperature dependence of ion permeation at the endplate channel. *J. Gen. Physiol.* **81**, 687–703 (1983).
20. Jiang, Y., Idikuda, V., Chowdhury, S. & Chanda, B. Activation of the archaeal ion channel MthK is exquisitely regulated by temperature. *eLife* https://elifesciences.org/articles/59055 (2020).
21. Kufel, D. S. & Wojcik, G. M. Analytical modelling of temperature effects on an AMPA-type synapse. *J. Comput. Neurosci.* **44**, 379–391 (2018).
22. Singh, A. K. et al. Structural basis of temperature sensation by the TRP channel TRPV3. *Nat. Struct. Mol. Biol.* **26**, 994–998 (2019).
23. Nadezhdin, K. D. et al. Structural mechanism of heat-induced opening of a temperature-sensitive TRP channel. *Nat. Struct. Mol. Biol.* **28**, 564–572 (2021).
24. Kwon, D. H. et al. Heat-dependent opening of TRPV1 in the presence of capsaicin. *Nat. Struct. Mol. Biol.* **28**, 554–563 (2021).
25. Hu, J. et al. Physiological temperature drives TRPM4 ligand recognition and gating. *Nature* **630**, 509–515 (2024).
26. Chen, C.-Y., Chang, Y.-C., Lin, B.-L., Huang, C.-H. & Tsai, M.-D. Temperature-resolved cryo-EM uncovers structural bases of temperature-dependent enzyme functions. *J. Am. Chem. Soc.* **141**, 19983–19987 (2019).
27. Bansia, H. et al. Investigating gating mechanisms of ion channels using temperature-resolved cryoEM. *Microsc. Microanal.* **27**, 1690–1694 (2021).
28. Horning, M. S. & Mayer, M. L. Regulation of AMPA receptor gating by ligand binding core dimers. *Neuron* **41**, 379–388 (2004).
29. Armstrong, N., Jasti, J., Beich-Frandsen, M. & Gouaux, E. Measurement of conformational changes accompanying desensitization in an ionotropic glutamate receptor. *Cell* **127**, 85–97 (2006).
30. Zuo, J. et al. Neurodegeneration in Lurcher mice caused by mutation in delta2 glutamate receptor gene. *Nature* **388**, 769–773 (1997).
31. Wollmuth, L. P. et al. The Lurcher mutation identifies δ2 as an AMPA/kainate receptor-like channel that is potentiated by Ca2+. *J. Neurosci.* **20**, 5973–5980 (2000).
32. Schwarz, M. K. et al. Dominance of the lurcher mutation in heteromeric kainate and AMPA receptor channels. *Eur. J. Neurosci.* **14**, 861–868 (2001).

33. Taverna, F. et al. The Lurcher mutation of an alpha-amino-3-hydroxy-5-methyl-4-isoxazolepropionic acid receptor subunit enhances potency of glutamate and converts an antagonist to an agonist. *J. Biol. Chem.* **275**, 8475–8479 (2000).
34. Kohda, K., Wang, Y. & Yuzaki, M. Mutation of a glutamate receptor motif reveals its role in gating and delta2 receptor channel properties. *Nat. Neurosci.* **3**, 315–322 (2000).
35. Gangwar, S. P. et al. Kainate receptor channel opening and gating mechanism. *Nature* **630**, 762–768 (2024).
36. Sobolevsky, A. I., Yelshansky, M. V. & Wollmuth, L. P. The outer pore of the glutamate receptor channel has 2-fold rotational symmetry. *Neuron* **41**, 367–378 (2004).
37. Wollmuth, L. P. & Sobolevsky, A. I. Structure and gating of the glutamate receptor ion channel. *Trends Neurosci.* **27**, 321–328 (2004).
38. Bowie, D. Ionotropic glutamate receptors & CNS disorders. *CNS Neurol. Disord. Drug Targets* **7**, 129–143 (2008).
39. Huettner, J. E. Glutamate receptor pores. *J. Physiol.* **593**, 49–59 (2015).
40. Patneau, D., Vyklicky, L. & Mayer, M. Hippocampal neurons exhibit cyclothiazide-sensitive rapidly desensitizing responses to kainate. *J. Neurosci.* **13**, 3496–3509 (1993).
41. Sun, Y. et al. Mechanism of glutamate receptor desensitization. *Nature* **417**, 245–253 (2002).
42. Stern-Bach, Y., Russo, S., Neuman, M. & Rosenmund, C. A point mutation in the glutamate binding site blocks desensitization of AMPA receptors. *Neuron* **21**, 907–918 (1998).
43. Klykov, O., Gangwar, S. P., Yelshanskaya, M. V., Yen, L. & Sobolevsky, A. I. Structure and desensitization of AMPA receptor complexes with type II TARP γ5 and GSG1L. *Mol Cell* **81**, 4771–4783.e7 (2021).
44. Amin, J. B. et al. Two gates mediate NMDA receptor activity and are under subunit-specific regulation. *Nat. Commun.* **14**, 1623 (2023).
45. Amin, J. B., Leng, X., Gochman, A., Zhou, H.-X. & Wollmuth, L. P. A conserved glycine harboring disease-associated mutations permits NMDA receptor slow deactivation and high Ca^{2+} permeability. *Nat. Commun.* **9**, 3748 (2018).
46. Salpietro, V. et al. AMPA receptor GluA2 subunit defects are a cause of neurodevelopmental disorders. *Nat. Commun.* **10**, 3094 (2019).
47. Carrillo, E. et al. Memantine inhibits calcium-permeable AMPA receptors. Preprint at *bioRxiv* https://doi.org/10.1101/2024.07.02.601784 (2024).
48. Yelshanskaya, M. V. et al. Structural bases of noncompetitive inhibition of AMPA-subtype ionotropic glutamate receptors by antiepileptic drugs. *Neuron* **91**, 1305–1315 (2016).
49. Chou, T.-H. et al. Molecular mechanism of ligand gating and opening of NMDA receptor. *Nature* **632**, 209–217 (2024).
50. Zhao, Y., Chen, S., Swensen, A. C., Qian, W.-J. & Gouaux, E. Architecture and subunit arrangement of native AMPA receptors elucidated by cryo-EM. *Science* **364**, 355–362 (2019).
51. Zhang, D. et al. Structural mobility tunes signalling of the GluA1 AMPA glutamate receptor. *Nature* https://doi.org/10.1038/s41586-023-06528-0 (2023).
52. Ivica, J. et al. Proton-triggered rearrangement of the AMPA receptor N-terminal domains impacts receptor kinetics and synaptic localization. *Nat. Struct. Mol. Biol.* **31**, 1601–1613 (2024).
53. Prieto, M. L. & Wollmuth, L. P. Gating modes in AMPA receptors. *J. Neurosci.* **30**, 4449–4459 (2010).
54. Carbone, A. L. & Plested, A. J. R. Superactivation of AMPA receptors by auxiliary proteins. *Nat. Commun.* **7**, 10178 (2016).

Methods

Construct design

The GluA2–γ2 construct has been well characterized and used in previous studies[6,10–13,47,55,56]. In brief, rat $GluA2_{flip}$ (GluA2* construct, from ref. 57) was fused to the amino terminus (NT) of mouse TARPγ2 (NP_031609, carboxy terminus (CT) truncated after L207/TM4). There is a single Gly-Thr spacer between the CT of GluA2* and NT of TARPγ2. After TARPγ2 there is a Thr-Gly-Gly spacer, thrombin cleavage site, enhanced green fluorescent protein for FSEC and monitoring expression, StrepTagII and stop codon. GluA2–γ2 is in the pEG BacMam vector for baculovirus-driven protein expression in mammalian cells[58].

Electrophysiology

Human embryonic kidney 293T cells were plated in poly-D-lysine-coated 35-mm dishes and transfected with GluA2–γ2 (construct described above for cryo-EM) or rat $GluA2_{flip}$ (Q) alone or with rat $GluA2_{flip}$ (Q) and rat γ2 coexpressed at the ratio of 1:1. Recordings were performed in the outside-out patch-clamp configuration. Pipettes with 8–15 MΩ resistance were filled with 135 mM CsF, 33 mM CsOH, 2 mM $MgCl_2$, 1 mM $CaCl_2$, 11 mM EGTA, 10 mM HEPES. The external solution was as follows: 150 mM NaCl, 4 mM KCl, 2 mM $CaCl_2$, 10 mM HEPES and 10 mM glutamate, pH 7.4. Data were acquired at 50 kHz and low-pass filtered at 5–10 kHz (Axon 200B and Digidata 1550A; Molecular Devices; collected with Clampex-10.7). Pipette holding potential was −100 mV. Data were further filtered at 1 kHz (ref. 14). All recordings were idealized using the segmental *k*-means algorithm of QuB[59,60]. The kinetic model used three closed and two open levels. After the idealized recording was visually inspected and noise spikes were removed, open and shut times were exported to the Channel Lab program (Synaptosoft), and histograms of the dwell times were shown and fitted with log-likelihood log-binned subroutines[15]. The mean open time, mean shut time and open probability were obtained using Channel Lab with an imposed dead time of 100 μs. Temperature control was achieved with a micro heating VAHEAT stage (Interherence GmbH), in addition to a glutamate solution maintained in water baths at each temperature step. To verify temperature, the temperature near the patch was recorded with a BAT-12 Microprobe Thermometer (Physitemp Instruments, LLC) within 5 mm of the microelectrode tip. Details can be found in source data. Glutamate maintained at the recording temperature was added to the bath through a Warner instrument (SF-77B) step perfusion device and glutamate was present throughout the recording. Segments of the single channel recording in which the temperature was constant at the desired temperature were used for the analysis. Q_{10} was calculated based on the ratio of the rate or conductance at temperatures different by 10 °C.

Protein expression and purification

The GluA2–γ2 bacmid was generated following the method described previously[13]. Following that, ExpiSf9 Cells (Gibco, A35243) cultured at 27 °C, were transfected with the bacmid using ExpiFectamine Sf transfection reagent (Gibco, A38915) to generate the P1 baculovirus. After 5 days, the culture supernatant of ExpiSf9 cells containing the P1 baculovirus was collected.

The P1 baculovirus supernatant was added to the Expi293F GnTI$^-$ cells (Gibco, A39240), maintained at 37 °C in 5% CO_2 in a 1:10 volume by volume ratio to commence the protein expression. After 16–18 h, the protein expression was induced by adding 10 mM sodium butyrate (Sigma-Aldrich, 303410) and transferring the cells to an incubator set at 30 °C, 5% CO_2. At this point, 2 μM ZK 20075 (Tocris, 2345) was also added to the cells. After 72 h of infection, the cells were collected by low-speed centrifugation (roughly 5,000*g*, 20 min, 4 °C). Cells were washed with 1× PBS (pH 7.4), pelleted again (roughly 5,000*g*, 20 min, 4 °C) and stored at −80 °C for further use.

For purification, the cell pellet was thawed by rotating in a Tris buffer solution (Tris 20 mM, NaCl 150 mM, pH 8.0) along with the protease inhibitors (0.8 μM aprotinin, 2 μg ml^{-1} leupeptin, 2 μM pepstatin A and 1 mM phenylmethylsulfonyl fluoride). The cells were lysed using a blunt probe sonicator (Fisher Scientific) (3–4 cycles of 1 s on, 1 s off, roughly 20 W of power). Lysate was then clarified by low-speed centrifugation (roughly 2,500*g*, 20 min, 4 °C) and the membranes were pelleted by using ultracentrifugation (125,000*g*, 45 min, 4 °C). The pelleted membranes were resuspended, mechanically homogenized and solubilized in the solubilization buffer (150 mM NaCl, 20 mM Tris pH 8.0, 1% *n*-dodecyl-β-D-maltopyranoside (Anatrace, D310) and 0.2% cholesteryl hemisuccinate Tris salt (Anatrace, CH210) for 2 h at 4 °C with constant stirring. The insoluble material in the solubilized membranes was separated by ultracentrifugation (125,000*g*, 45 min, 4 °C) and the soluble fraction was incubated with the Strep-Tactin XT 4Flow resin (IBA, 2-5010) at 4 °C, rotating overnight. The following day, the protein-bound resin was collected by gravity flow and washed with the GDN buffer containing 20 mM Tris, 150 mM NaCl and 100 μM GDN (Anatrace, GDN101). The protein was eluted with the GDN buffer containing 50 mM Biotin (ThermoFisher, 29129), directly collected in a 100 kDa molecular weight cut-off filter and centrifugal concentrator, and concentrated up to roughly 500 μl in volume. The enhanced green fluorescent protein and StrepTagII were cleaved proteolytically, by incubating the protein with thrombin in a ratio of 1:100 (w/w) for 1 h at 25 °C. The sample was then subjected to size-exclusion chromatography by using a Superose 6 Increase 10/300 column (Cytiva, 29091596) equilibrated with the GDN buffer. The peak fractions were pooled, concentrated up to roughly 4 mg ml^{-1} and used for cryo-EM specimen preparation.

FSEC

Purified GluA2–γ2 was incubated at three different temperature conditions (at 4, 37 and 42 °C) for 15 min, separately and tested for stability by FSEC[61]. FSEC was carried out in a high-performance liquid chromatography system attached to a multi-wavelength fluorescence detector, an autosampler (Shimadzu, SIL40C) and a Superose 6 Increase 10/300 GL SEC column (Cytiva). The tryptophan fluorescence was used to monitor the protein stability and retention time (excitation at 280 nm and emission at 325 nm).

Cryo-EM sample preparation and data collection

Two types of grid were used. C-flat (CF-1.2/1.3-2Au-50, catalogue no. CF213-50-Au, Electron Microscopy Sciences) grids were coated with 50 nm Au by Sputter Coater Leica EM ACE600 and plasma cleaned with Ar/O_2 by Tergeo Plasma Cleaner (Pie Scientific) to make holey 1.2/1.3 gold grids with gold mesh based on published methods[12,62]. These homemade gold grids along with Au-Flat (GF-2/2-2Au-45nm-50, catalogue no. AUFT222-50, Electron Microscopy Sciences), were glow discharged in a Pelco Easiglow (25 mA, 120-s glow time and 10-s hold time; Ted Pella, 91000).

The purified GluA2–γ2 protein sample was ultracentrifuged to remove the insoluble material. 20 μl of the protein sample was then incubated on a heat block set at 37 or 42 °C for 10 min. The protein sample was then immediately spiked with 1 mM glutamate from a stock that was prewarmed on the 37 or 42 °C heat block (for the glutamate-bound sample), and 3 μl of the protein sample was applied to the freshly glow-discharged grids in a FEI Vitrobot Mark IV (ThermoFisher Scientific) chamber set at 37 or 42 °C temperature and 90% humidity and immediately plunge frozen in liquid ethane cooled by liquid nitrogen. For the apo-state GluA2–γ2 condition, the protein was directly applied on grids after incubating on the 42 °C heat block without spiking in any glutamate.

A total of 53,560 micrographs were collected for temperature-resolved cryo-EM. All data were collected on a Titan Krios G3i microscope (ThermoFisher Scientific) operating at 300 kV, equipped with

Falcon4i camera and selectris energy filter set at a 10 eV slit width. Data collection was performed in an automated manner using EPU software (ThermoFisher Scientific). For the glutamate-activated states, all activated state data were collected with a total dose of 40.00 $e^-/Å^2$, a dose rate of 8.56 e^- per pixel per s, and a pixel size of 0.97 Å per pixel. For the 37 °C dataset, 20,104 micrographs were collected, and 23,236 micrographs were collected for the 42 °C dataset. For the apo-state at 42 °C, 10,220 micrographs were collected with a total dose of 40.00 $e^-/Å^2$, a dose rate of 9.92 e^- per pixel per s and a pixel size of 0.97 Å per pixel. The defocus range was 1.0 to −2.5 µm for all the collections.

Image processing

CryoSPARC[63] (v.4.5.3) was primarily used for all aspects of image processing. Final particle picking was performed with TOPAZ[64]. Details can be found in Extended Data Figs. 3–6 and Extended Data Tables 1 and 2.

Model building, refinements and structural analysis

ChimeraX[65], ISOLDE[66], Coot[67] and PHENIX[68] compiled by the SBgrid Consortium[69] were used in combination to perform the model building, refinements and structural analysis. All visualizations and measurements were performed in ChimeraX. Model quality was assessed with MolProbity[70]. Pore measurements were performed with HOLE[71]. Model quality is reported in Extended Data Tables 1 and 2 and pore fits in Extended Data Fig. 7.

Multiple sequence alignment

Rat iGluR protein sequences were accessed from UniProt (Gria1, P19490; Gria2, P19491; Gria3, P19492; Gria4, P19493; Grik1, P22756; Grik2, P42260; Grik3, P42264; Grik4, Q01812; Grik5, Q63273; Grid1, Q62640; Grid2, Q63226; Nmdz1, P35439; Nmde1, Q00959; Nmde2, Q00960; Nmde3, Q00961; Nmde4, Q62645; Nmd3a, Q9R1M7; Nmd3b, Q8VHN2). Amino acid sequence alignments were generated using Clustal Omega[72] and were visualized with ESPript v.3.0 (ref. 73).

Reporting summary

Further information on research design is available in the Nature Portfolio Reporting Summary linked to this article.

Data availability

The cryo-EM reconstructions are deposited into the Electron Microscopy Data Bank. The LBD–TMD maps are the primary cryo-EM maps in each deposition and each TMD local map, as applicable, and half maps are supplied as supplementary files in each deposition. All protein models are deposited in the PDB. Access codes are as follows: 37 °C data: activated (EMD-48557, PDB 9MRK), desensitized-1 (EMD-48558, PDB 9MRL) and desensitized-2 (EMD-48559, PDB 9MRM); 42 °C data: resting-1 (EMD-46872, PDB 9DHP), resting-2 (EMD-46873, PDB 9DHQ), activated (EMD-46874, PDB 9DHR), desensitized-1 (EMD-46875, PDB 9DHS) and desensitized-2 (EMD-46876, PDB 9DHT). Consensus activated state is at EMD-48560 and PDB 9MRN. All electrophysiology data are included in the main paper and Extended Data Fig. 1. Source data are provided with this paper.

55. Twomey, E. C., Yelshanskaya, M. V., Grassucci, R. A., Frank, J. & Sobolevsky, A. I. Structural bases of desensitization in AMPA receptor-auxiliary subunit complexes. *Neuron* **94**, 569–580.e5 (2017).
56. Hale, W. D. et al. Structure of transmembrane AMPA receptor regulatory protein subunit γ2. *Nat. Commun.* **16**, 671 (2025).
57. Yelshanskaya, M. V., Li, M. & Sobolevsky, A. I. Structure of an agonist-bound ionotropic glutamate receptor. *Science* **345**, 1070–1074 (2014).
58. Goehring, A. et al. Screening and large-scale expression of membrane proteins in mammalian cells for structural studies. *Nat. Protoc.* **9**, 2574–2585 (2014).
59. Qin, F. Restoration of single-channel currents using the segmental k-means method based on hidden Markov modeling. *Biophys. J.* **86**, 1488–1501 (2004).
60. Nicolai, C. & Sachs, F. Solving ion channel kinetics with the qub software. *Biophys. Rev. Lett.* **08**, 191–211 (2013).
61. Kawate, T. & Gouaux, E. Fluorescence-detection size-exclusion chromatography for precrystallization screening of integral membrane proteins. *Structure* **14**, 673–681 (2006).
62. Russo, C. J. & Passmore, L. A. Ultrastable gold substrates for electron cryomicroscopy. *Science* **346**, 1377–1380 (2014).
63. Punjani, A., Rubinstein, J. L., Fleet, D. J. & Brubaker, M. A. cryoSPARC: algorithms for rapid unsupervised cryo-EM structure determination. *Nat. Methods* **14**, 290–296 (2017).
64. Bepler, T. et al. Positive-unlabeled convolutional neural networks for particle picking in cryo-electron micrographs. *Nat. Methods* **16**, 1153–1160 (2019).
65. Pettersen, E. F. et al. UCSF ChimeraX: structure visualization for researchers, educators, and developers. *Protein Sci.* **30**, 70–82 (2021).
66. Croll, T. I. ISOLDE: a physically realistic environment for model building into low-resolution electron-density maps. *Acta Crystallogr. D Struct. Biol.* **74**, 519–530 (2018).
67. Emsley, P. & Cowtan, K. Coot: model-building tools for molecular graphics. *Acta Cryst. D* **60**, 2126–2132 (2004).
68. Liebschner, D. et al. Macromolecular structure determination using X-rays, neutrons and electrons: recent developments in Phenix. *Acta Cryst. D* **75**, 861–877 (2019).
69. Morin, A. et al. Collaboration gets the most out of software. *eLife* **2**, e01456 (2013).
70. Williams, C. J. et al. MolProbity: more and better reference data for improved all-atom structure validation. *Protein Sci.* **27**, 293–315 (2018).
71. Smart, O. S., Neduvelil, J. G., Wang, X., Wallace, B. A. & Sansom, M. S. P. HOLE: a program for the analysis of the pore dimensions of ion channel structural models. *J. Mol. Graphics* **14**, 354–360 (1996).
72. Sievers, F. & Higgins, D. G. Clustal Omega for making accurate alignments of many protein sequences. *Protein Sci.* **27**, 135–145 (2018).
73. Gouet, P., Robert, X. & Courcelle, E. ESPript/ENDscript: extracting and rendering sequence and 3D information from atomic structures of proteins. *Nucleic Acids Res.* **31**, 3320–3323 (2003).

Acknowledgements We thank A. Lau (JHU) and Z. Qiu (JHU) for comments on the manuscript, and W. D. Hale, A. Montaño Romero and L. Dillard (Twomey Laboratory) for critical insights during the development of this work. We thank J. F. Cordero-Morales (UTHSC) for lending the VAHEAT micro heating stage used in this work. All cryo-EM data were collected at the Beckman Center for Cryo-EM at Johns Hopkins. E.C.T. is supported by National Institutes of Health (NIH) grant no. R35GM154904, the Searle Scholars Program (Kinship Foundation grant no. 22098168) and the Diana Helis Henry Medical Research Foundation (grant no. 142548). V.J. is supported by NIH grant no. R35GM122528.

Author contributions E.C.T. conceptualized and supervised the project. A.K.M., E.C., V.J. and E.C.T. designed the experiments. A.K.M. performed protein expression, purification and specimen preparation for cryo-EM. A.K.M. collected the cryo-EM data. A.K.M. and E.C.T. processed the cryo-EM data. E.C.T. built the molecular models. E.C. and V.J. designed the electrophysiology experiments. E.C. performed the electrophysiology experiments. E.C. and V.J. performed the electrophysiology data analysis. A.K.M. and E.C.T. wrote the manuscript, which was then edited by all authors.

Competing interests The authors declare no competing interests.

Additional information

Supplementary information The online version contains supplementary material available at https://doi.org/10.1038/s41586-025-08770-0.

Correspondence and requests for materials should be addressed to Vasanthi Jayaraman or Edward C. Twomey.

Peer review information *Nature* thanks Andrew Plested, Gabriela Popescu and Shujia Zhu for their contribution to the peer review of this work. Peer reviewer reports are available.

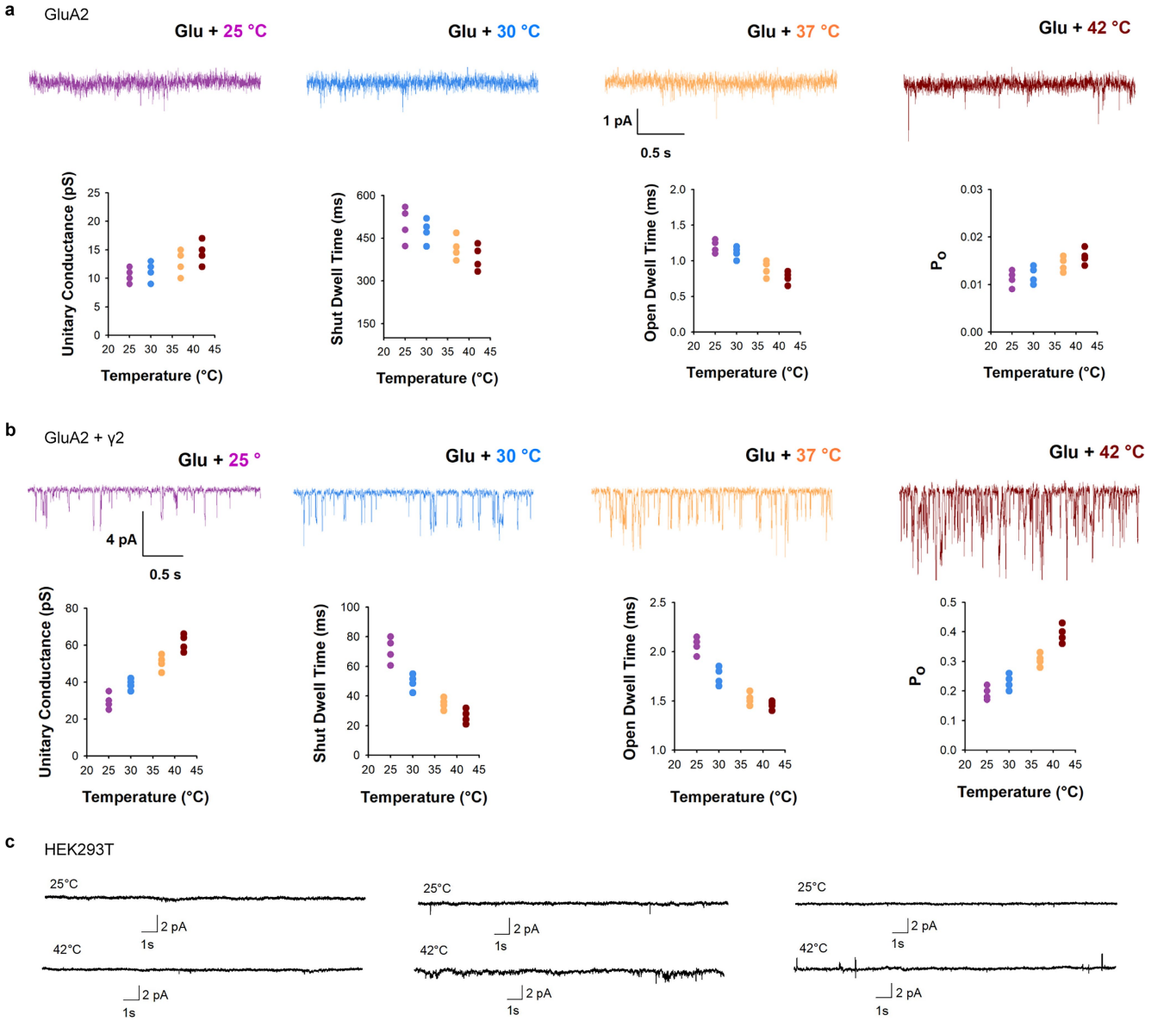

Extended Data Fig. 1 | Single channel currents for GluA2 and GluA2 with γ2 at physiological temperatures. For **a** (GluA2 transfected cells) and **b** (cells co-transfected with GluA2 and γ2): example single channel currents at 25 °C, 30 °C, 37 °C, and 42 °C recorded on a single membrane patch in the presence of 10 mM glutamate (Glu). Average unitary conductance, average closed dwell time, open dwell time, channel open probability (P_O) for single channel membrane patches at each temperature. For GluA2 single channel membrane patches at each temperature (n = 4 patch current recordings for each 25 °C, 30 °C, 37 °C, 42 °C). The amplitude events were recorded for 1-2 min at each temperature step per patch. The total times recorded for each temperature step were: 8 min (25 °C), 8 min (30 °C), 8 min (37 °C), and 6 min (42 °C). For GluA2 + γ2 single channel membrane patches at each temperature (n = 4 patch current recordings for each 25 °C, 30 °C, 37 °C, 42 °C). The amplitude events were recorded for 1-2 min at each temperature step per patch. The total times recorded for each temperature step were: 8 min (25 °C), 8 min (30 °C), 7 min (37 °C), and 6 min (42 °C). **c**, three separate patches where currents were recorded at 25 °C and 42 °C in the presence of 10 mM glutamate from HEK293T cells not transfected.

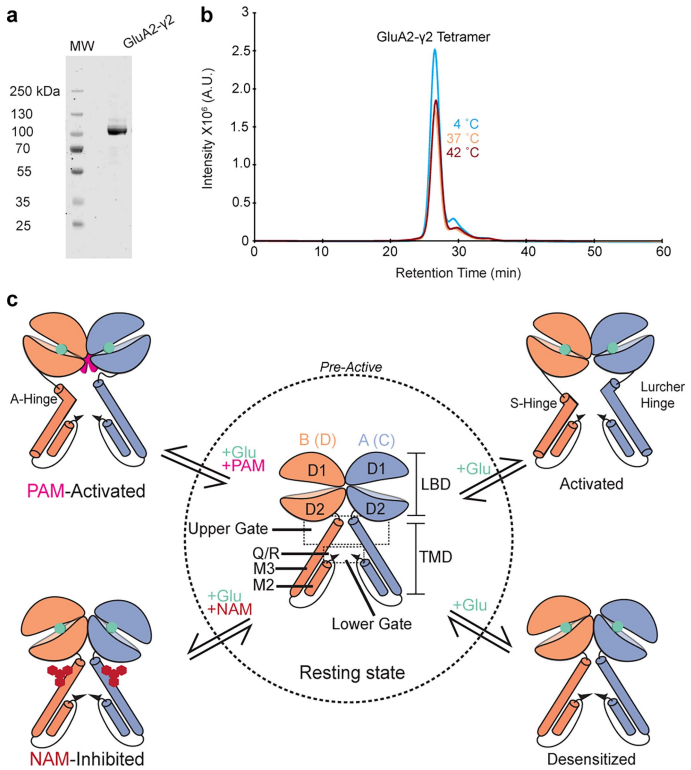

Extended Data Fig. 2 | Purification and stability of GluA2-γ2 at physiological temperatures, gating and allostery model. a, SDS-PAGE of purified GluA2-γ2. Molecular weight marker (left), GluA2-γ2 (right). For source data, see Supplementary Fig. 1. **b**, FSEC tryptophan fluorescence chromatograms of purified GluA2-γ2 at 4 °C, 37 °C, and 42 °C. **c**, Summary of AMPAR allostery and gating. Transitioning between conformational states of the AMPAR is facilitated by the pre-active intermediate (dashed line). Temperature increases transition probabilities between the resting, activated, and desensitized states. The PAM-activated and NAM-inhibited states are distinct from the normal glutamate gating cycle.

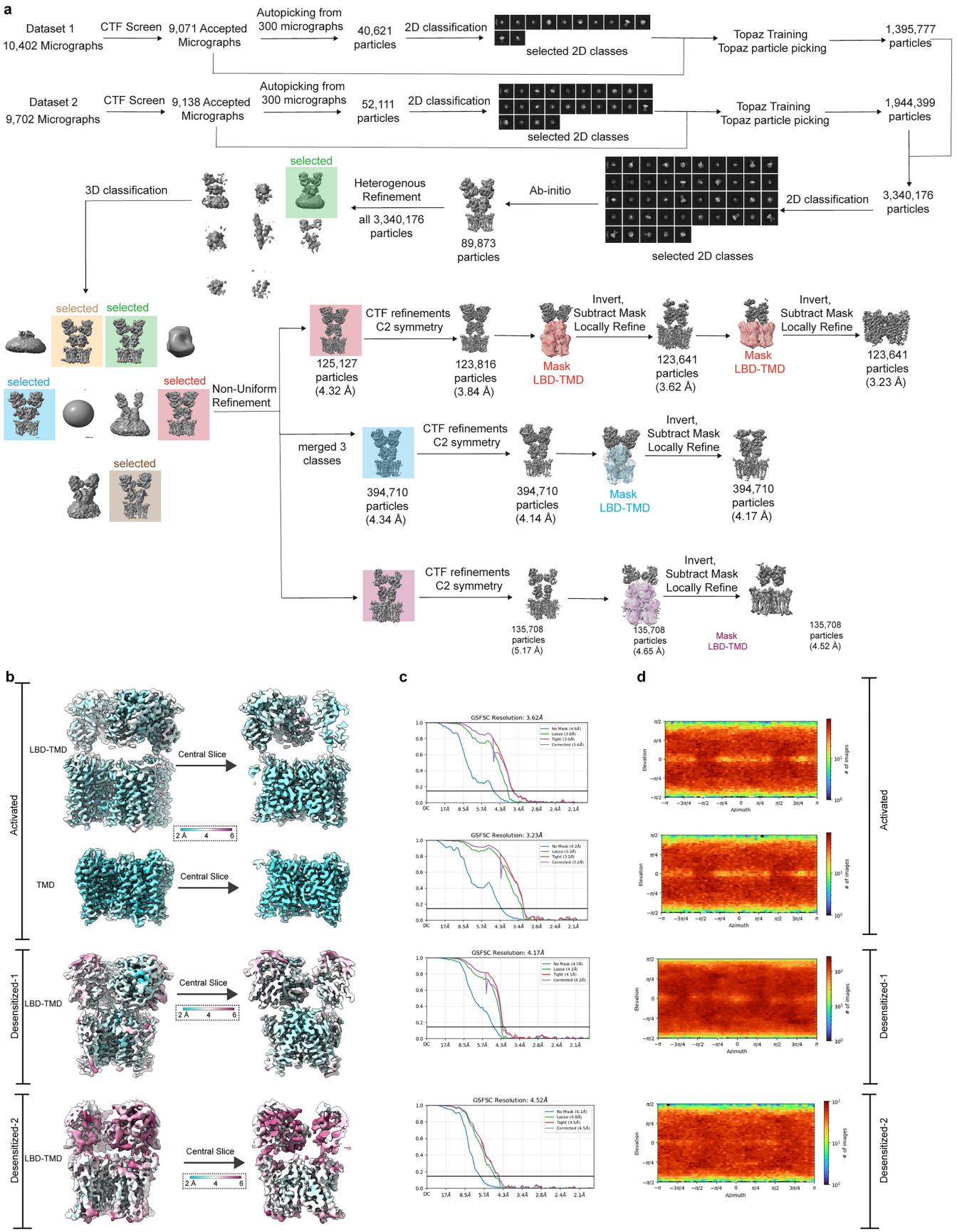

Extended Data Fig. 3 | Cryo-EM image processing for Glu-37 °C data. **a**, workflow in Cryosparc. **b**, local resolution maps computed for each voxel, where resolutions were computed at Fourier shell correlation (FSC) = 0.143. **c**, gold standard Fourier shell correlation (GSFSC) curves for each map. Black line is FSC = 0.143. Y axis is FSC, X is resolution in Å. **d**, heat maps of particle orientation distribution for each map.

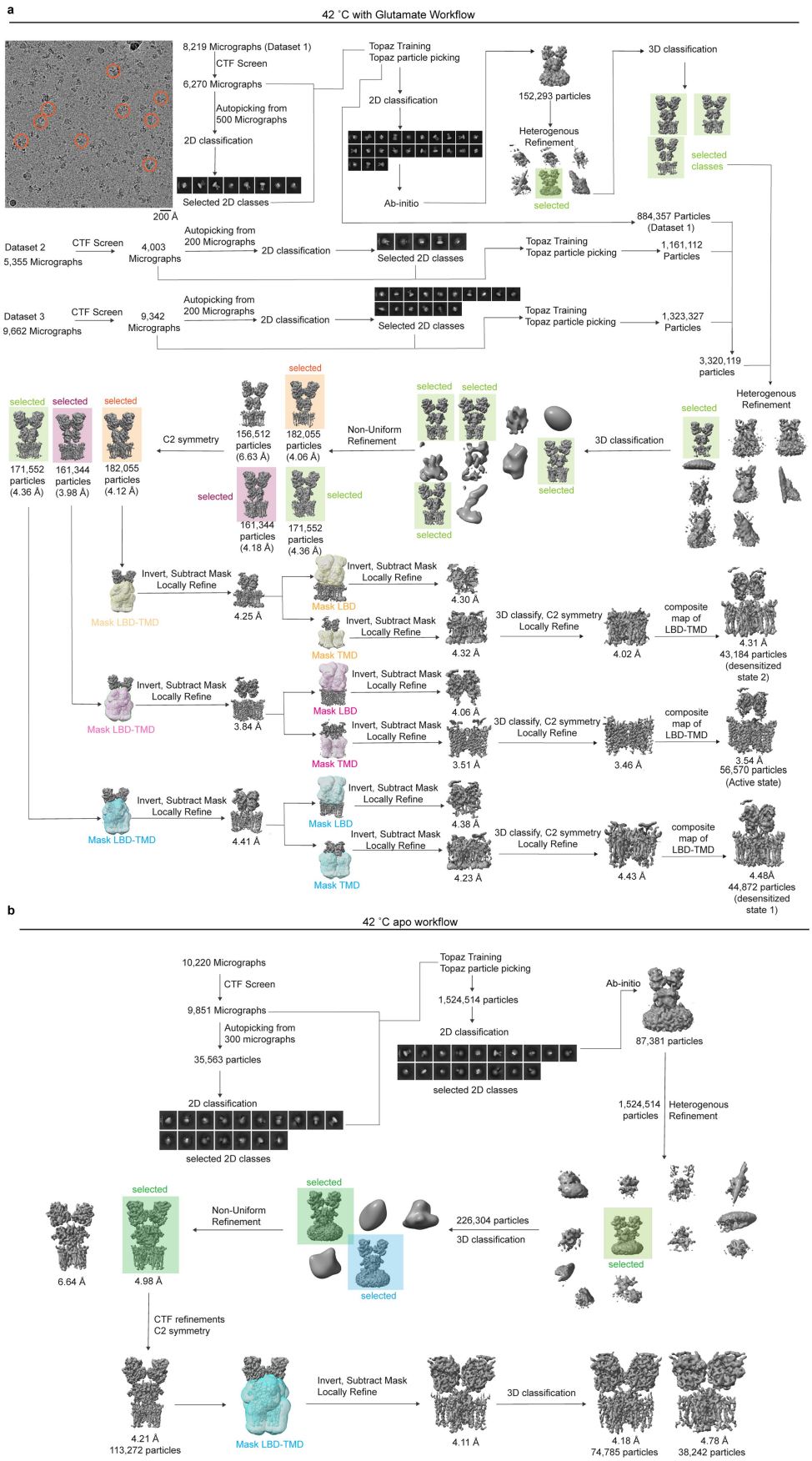

Extended Data Fig. 4 | Cryo-EM image processing of 42 °C data. a, workflow in Cryosparc for the 42 °C glutamate data. **b**, workflow in Cryosparc for the 42 °C data without glutamate.

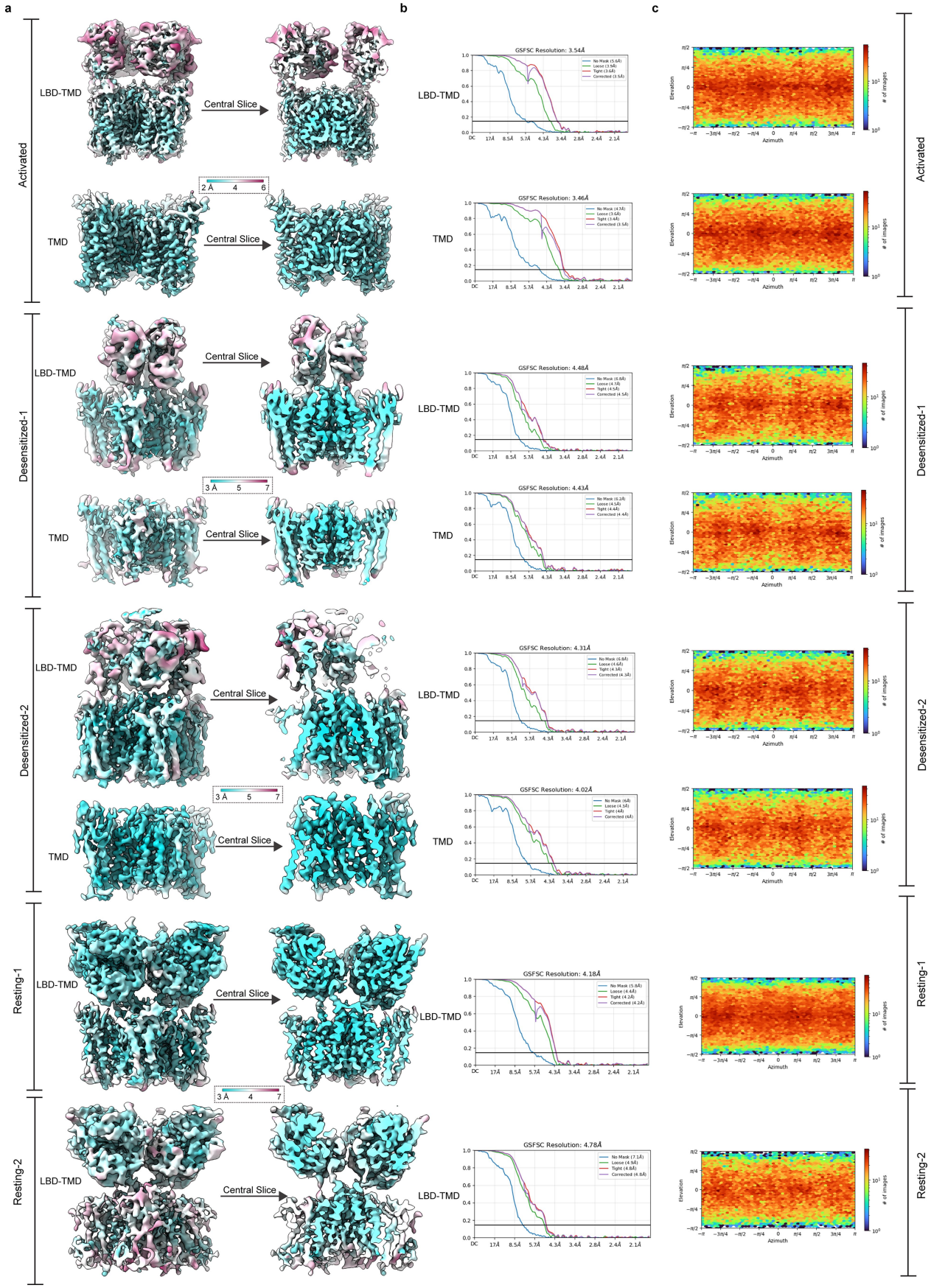

Extended Data Fig. 5 | Local and overall map qualities for 42 °C cryo-EM data. a, local resolution maps computed for each voxel, where resolutions were computed at FSC = 0.143. **b**, GSFSC curves for each map. Black line is FSC = 0.143. Y axis is FSC, X is resolution in Å. **c**, heat maps of particle orientation distribution for each map.

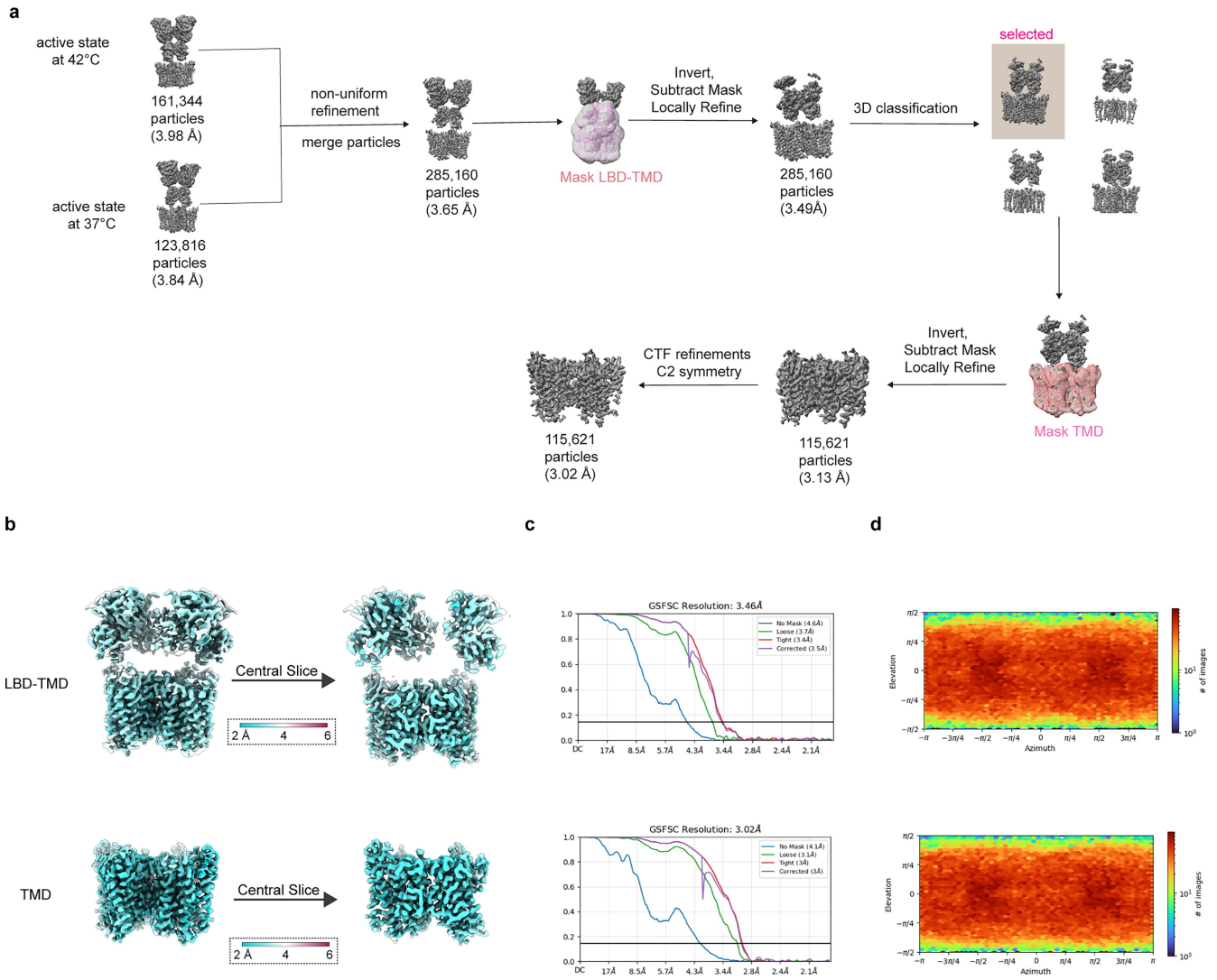

Extended Data Fig. 6 | Consensus activated state workflow, map local quality, and overall quality. a, image processing workflow. **b**, local resolution maps computed for each voxel, where resolutions were computed at FSC = 0.143. **c**, GSFSC curves for each map. Black line is FSC = 0.143. Y axis is FSC, X is resolution in Å. d, heat maps of particle orientation distribution for each map.

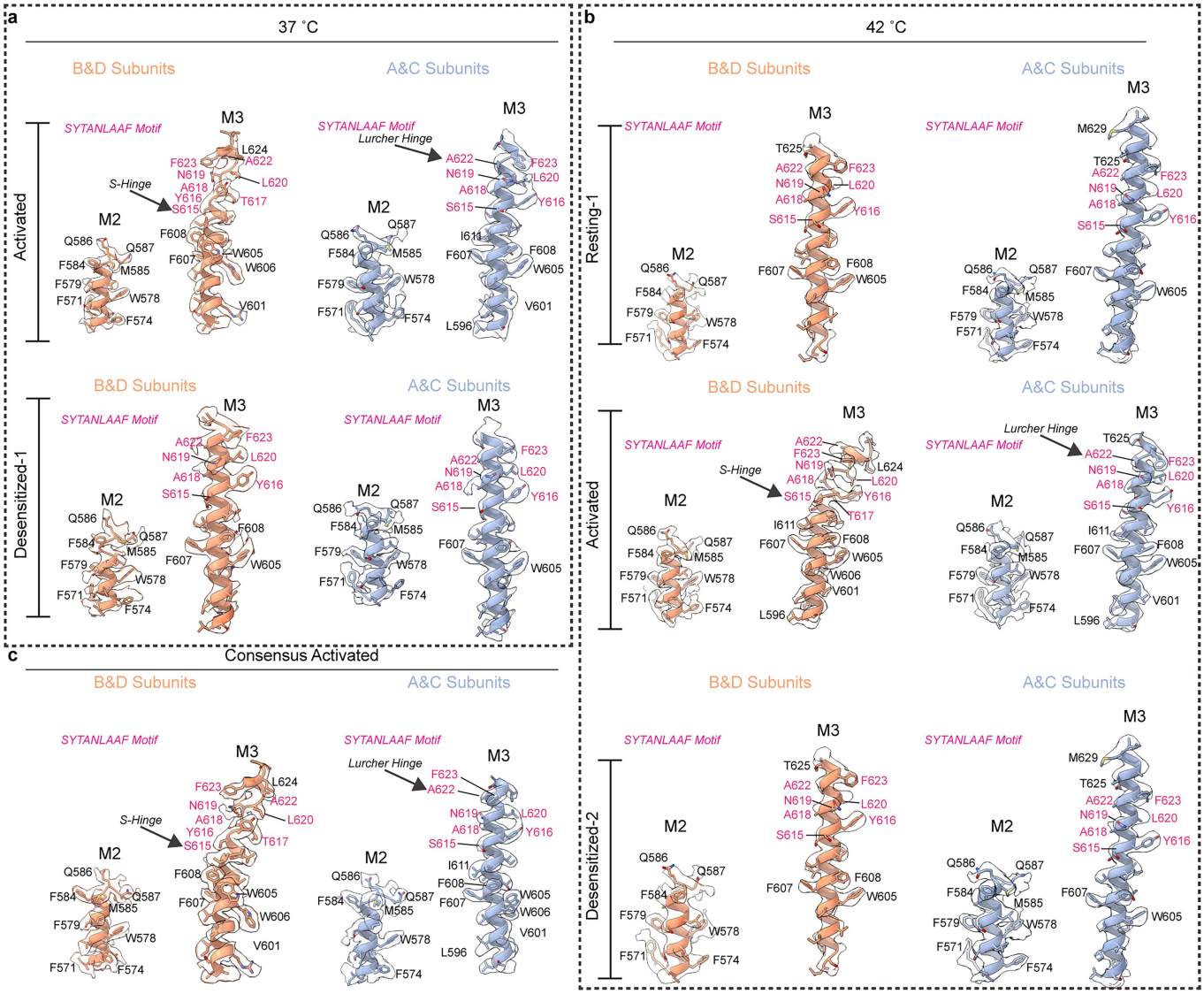

Extended Data Fig. 7 | Pore helix map quality and model fit. a, 37 °C desensitized-1, and activated state M2 and M3 model-map fit, B&D subunits on left, A&C subunits right. **b**, 42 °C Resting -1, activated state, and desensitized-2 M2 and M3 model-map fit, B&D subunits on left, A&C subunits right. **c**, Consensus activated state M2 and M3 model-map fit, B&D subunits on left, A&C subunits right. Residues that are part of the SYTANLAAF motif are labeled in pink.

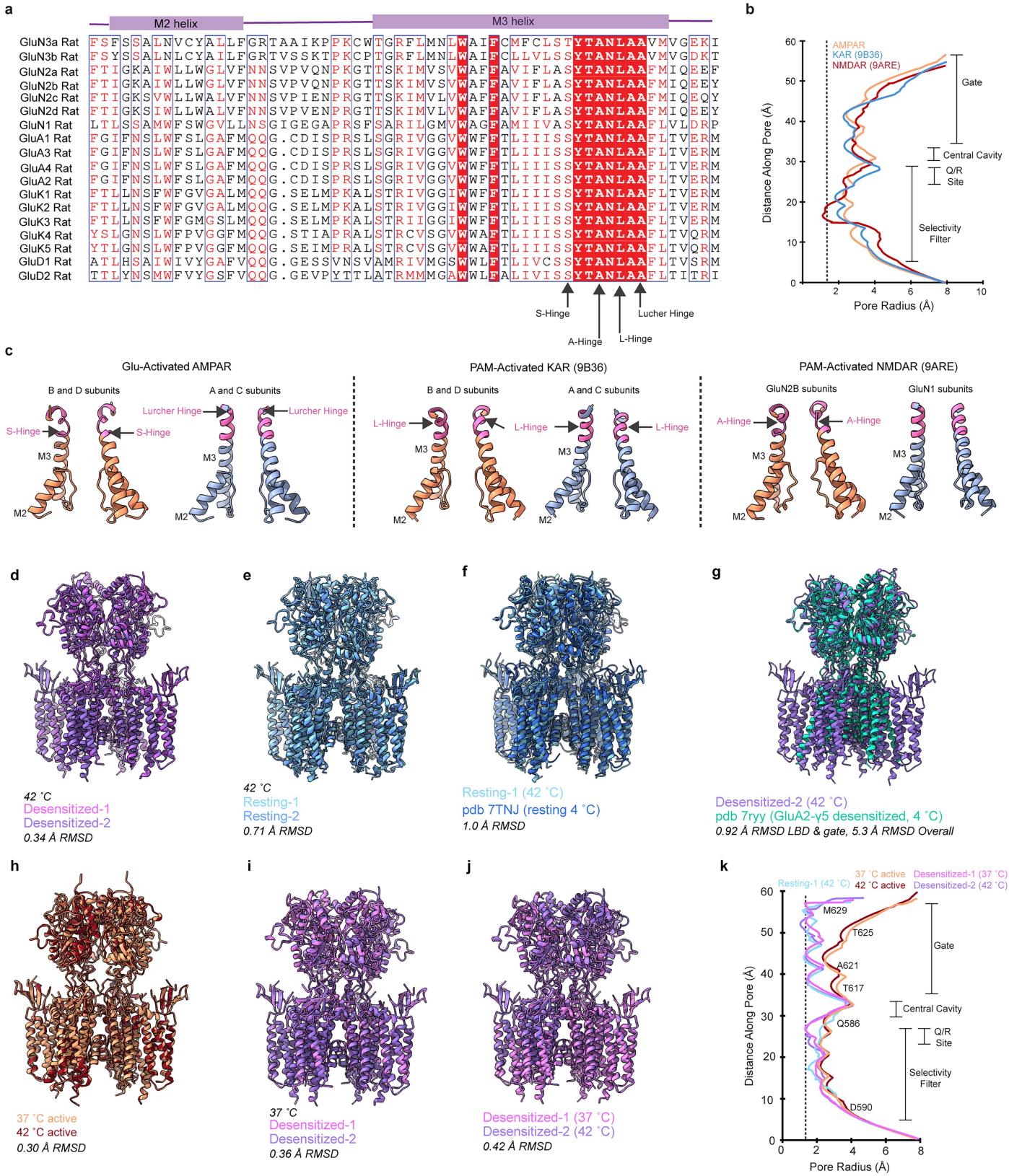

Extended Data Fig. 8 | Conserved pore motifs in iGluRs, pore features of activated iGluRs, and structural comparisons. a, Amino acid sequence alignment of major iGluR families. **b**, Pore profiles of PAM-activated KAR (pdb 9B36) and PAM-activated NMDAR (pdb 9ARE) compared to the glutamate-activated state from this study. **c**, Pore hinging in structures plotted in panel B. Hinging locations are also marked in panel a. **d**, Structural alignment between Desensitized-1 and -2. **e**, Structural alignment between Resting-1 and -2. **f**, Structural alignment between Resting-1 and GluA2-γ2 resting prepared at 4 °C (pdb 7TNJ). **g**, Structural alignment between 42 °C desensitized-2 and GluA2-γ5 desensitized prepared at 4 °C (pdb 7RYY). **h**, structural alignment between 37 °C and 42 °C GluA2-γ2 activated states. **i**, Structural alignment between 37 °C desensitized-1 and -2 states. **j**, Structural alignment between 37 °C desensitized-1 and 42 °C desensitized-2 states. **k**, Pore profiles from 37 °C activated state, 37 °C desensitized -1, 42 °C resting-1, 42 °C activated state, 42 °C desensitized-2, and consensus activated state. Dashed line represents the radius of water, 1.4 Å.

Extended Data Table 1 | 37 °C cryo-EM data collection, refinement, and validation statistics, including consensus activated state

	Activated (EMD-48557) (PDB 9MRK)	Desensitized-1 (EMD-48558) (PDB 9MRL)	Desensitized-2 (EMD-48559) (PDB 9MRM)	Consensus Activated (EMD-48560) (PDB 9MRN)
Data collection and processing				
Magnification	130,000x	130,000x	130,000x	130,000x
Voltage (kV)	300	300	300	300
Electron exposure (e–/Å^2)	40	40	40	40
Defocus range (μm)	-1.0 – 2.5	-1.0 – 2.5	-1.0 – 2.5	-1.0 – 2.5
Pixel size (Å)	0.97	0.97	0.97	0.97
Symmetry imposed	C2	C2	C2	C2
Initial particle images (no.)	3,340,176	3,340,176	3,340,176	285,160
Final particle images (no.)	123,641	394,710	135,708	115,621
Map resolution (Å) FSC = 0.143	3.62	4.17	4.52	3.46
Map resolution range (Å)	2.3 – 11.5	2.3 – 13.6	2.8 – 15.8	2.1 – 29.3
Refinement				
Initial model used (PDB code)	5WEO	5WEO	5WEO	5WEO
Model resolution (Å) FSC = 0.143	3.6	4.1	4.3	3.5
Model resolution range (Å)	3.5 – 3.8	3.9 – 4.3	4.1 – 4.5	3.4 – 3.6
Map sharpening *B* factor (Å^2)	-100	-174	-210	-77
Model composition				
Non-hydrogen atoms	18304	18296	18296	18304
Protein residues	2350	2350	2350	2350
Ligands				
B factors (Å^2)				
Protein	13.27/134.70/60.39	0.00/97.00/57.81	17.89/357.01/155.75	2.02/168.55/65.25
Ligand				
R.m.s. deviations				
Bond lengths (Å)	0.003	0.004	0.003	0.005
Bond angles (°)	0.574	0.675	0.649	0.773
Validation				
MolProbity score	1.32	1.48	1.502	1.45
Clashscore	2.37	3.84	3.98	2.23
Poor rotamers (%)	0	0	0	0.61
Ramachandran plot				
Favored (%)	95.69	95.60	95.60	96.39
Allowed (%)	4.14	4.14	4.10	3.48
Disallowed (%)	0.17	0.26	0.30	0.13

Extended Data Table 2 | 42 °C cryo-EM data collection, refinement, and validation statistics

	Resting-1 (EMD-46872) (PDB 9DHP)	Resting-2 (EMD-46873) (PDB 9DHQ)	Activated (EMD-46874) (PDB 9DHR)	Desensitized-1 (EMD-46875) (PDB 9DHS)	Desensitized-2 (EMD-46876) (PDB 9DHT)
Data collection and processing					
Magnification	130,000x	130,000x	130,000x	130,000x	130,000x
Voltage (kV)	300	300	300	300	300
Electron exposure (e–/Å^2)	40	40	40	40	40
Defocus range (μm)	-1.0 – 2.5	-1.0 – 2.5	-1.0 – 2.5	-1.0 – 2.5	-1.0 – 2.5
Pixel size (Å)	0.97	0.97	0.97	0.97	0.97
Symmetry imposed	C2	C2	C2	C2	C2
Initial particle images (no.)	1,524,514	1,524,514	3,320,119	3,320,119	3,320,119
Final particle images (no.)	74,785	38,242	56,570	44,872	43,184
Map resolution (Å) FSC = 0.143	4.18	4.78	3.54	4.48	4.31
Map resolution range (Å)	2.6 – 15.0	2.9 – 12.3	2.3 – 11.0	2.8 – 12.9	2.5 – 12.1
Refinement					
Initial model used (PDB code)	5WEO	5WEO	5WEO	5WEO	5WEO
Model resolution (Å) FSC = 0.143	4.3	4.8	3.7	4.5	4.3
Model resolution range (Å)	3.8 – 4.3	3.8 – 4.7	3.4 – 3.7	4.2 – 4.5	3.9 – 4.4
Map sharpening *B* factor (Å^2)	-137	-151	-94	-150	-134
Model composition					
Non-hydrogen atoms	18075	18075	18304	18296	18296
Protein residues	2328	2328	2350	2350	2350
Ligands					
B factors (Å^2)					
Protein	9.79/157.56/70.15	33.9/254.14/135.00	5.32/246.11/135.00	126.66/328.61/229.51	12.51/196.38/94.31
Ligand					
R.m.s. deviations					
Bond lengths (Å)	0.003	0.002	0.014	0.003	0.003
Bond angles (°)	0.670	0.714	0.837	0.714	0.665
Validation					
MolProbity score	1.52	1.55	1.45	1.53	1.47
Clashscore	3.23	3.17	3.1	3.11	2.94
Poor rotamers (%)	0.16	0	0.72	0.2	0.31
Ramachandran plot					
Favored (%)	93.98	93.01	95.03	93.52	94.30
Allowed (%)	5.84	6.51	4.62	5.79	5.35
Disallowed (%)	0.18	0.48	0.35	0.69	0.35

nature portfolio

Corresponding author(s): Twomey, Jayaraman

Last updated by author(s): Jan 26, 2025

Reporting Summary

Nature Portfolio wishes to improve the reproducibility of the work that we publish. This form provides structure for consistency and transparency in reporting. For further information on Nature Portfolio policies, see our Editorial Policies and the Editorial Policy Checklist.

Statistics

For all statistical analyses, confirm that the following items are present in the figure legend, table legend, main text, or Methods section.

n/a	Confirmed
☐	☒ The exact sample size (*n*) for each experimental group/condition, given as a discrete number and unit of measurement
☐	☒ A statement on whether measurements were taken from distinct samples or whether the same sample was measured repeatedly
☐	☒ The statistical test(s) used AND whether they are one- or two-sided *Only common tests should be described solely by name; describe more complex techniques in the Methods section.*
☒	☐ A description of all covariates tested
☐	☒ A description of any assumptions or corrections, such as tests of normality and adjustment for multiple comparisons
☐	☒ A full description of the statistical parameters including central tendency (e.g. means) or other basic estimates (e.g. regression coefficient) AND variation (e.g. standard deviation) or associated estimates of uncertainty (e.g. confidence intervals)
☒	☐ For null hypothesis testing, the test statistic (e.g. *F*, *t*, *r*) with confidence intervals, effect sizes, degrees of freedom and *P* value noted *Give P values as exact values whenever suitable.*
☒	☐ For Bayesian analysis, information on the choice of priors and Markov chain Monte Carlo settings
☒	☐ For hierarchical and complex designs, identification of the appropriate level for tests and full reporting of outcomes
☒	☐ Estimates of effect sizes (e.g. Cohen's *d*, Pearson's *r*), indicating how they were calculated

Our web collection on statistics for biologists contains articles on many of the points above.

Software and code

Policy information about availability of computer code

Data collection	EPU-3.5 (ThermoFisher), Clampex-10.7 (Molecular Devices)
Data analysis	Cryosparc- 4.2.1, ChimeraX-1.5, Isolde-1.6, COOT-0.9. 8.2, Phenix-1.20, Channellab-2.170219 (Synaptosoft)

For manuscripts utilizing custom algorithms or software that are central to the research but not yet described in published literature, software must be made available to editors and reviewers. We strongly encourage code deposition in a community repository (e.g. GitHub). See the Nature Portfolio guidelines for submitting code & software for further information.

Data

Policy information about availability of data

All manuscripts must include a data availability statement. This statement should provide the following information, where applicable:

- Accession codes, unique identifiers, or web links for publicly available datasets
- A description of any restrictions on data availability
- For clinical datasets or third party data, please ensure that the statement adheres to our policy

The cryo-EM reconstructions are deposited into the Electron Microscopy Data Bank (EMDB) and will be released upon publication. The LBD-TMD maps are the primary cryo-EM maps in each deposition and each TMD local map, as applicable, and half maps are supplied as supplemental files in each deposition. All protein models are deposited in the protein data bank (PDB) and will be released upon publication. Access codes are as follows: 37℃ Data: Activated (EMD-48557, PDB 9MRK). Desensitized-1 (EMD-48558, PDB 9MRL) Desensitized-2 (EMD-48559, PDB 9MRM). 42℃ Data: Resting-1 (EMD-46872, PDB 9DHP), Resting-2 (EMD-46873,

PDB 9DHQ), Activated (EMD-46874, PDB 9DHR). Desensitized-1 (EMD-46875, PDB 9DHS) Desensitized-2 (EMD-46876, PDB 9DHT). Consensus activated state is at EMD-48560 and PDB 9MRN. All electrophysiology data are included in main manuscript, extended data, and source data.

Research involving human participants, their data, or biological material

Policy information about studies with human participants or human data. See also policy information about sex, gender (identity/presentation), and sexual orientation and race, ethnicity and racism.

Reporting on sex and gender	N/A
Reporting on race, ethnicity, or other socially relevant groupings	N/A
Population characteristics	N/A
Recruitment	N/A
Ethics oversight	N/A

Note that full information on the approval of the study protocol must also be provided in the manuscript.

Field-specific reporting

Please select the one below that is the best fit for your research. If you are not sure, read the appropriate sections before making your selection.

☒ Life sciences ☐ Behavioural & social sciences ☐ Ecological, evolutionary & environmental sciences

For a reference copy of the document with all sections, see nature.com/documents/nr-reporting-summary-flat.pdf

Life sciences study design

All studies must disclose on these points even when the disclosure is negative.

Sample size	Cryo-EM sample size was not predetermined prior to study, but was determined by the availability of microscope time. Sample size for current recordings was predetermined to be at least three for statistical reasons. Recording duration at each temperature step was performed for 1-2 minutes depending on patch. Patches were only taken from cells if they fluoresced green from the cryo-EM construct.
Data exclusions	No data was excluded.
Replication	Image processing in cryo-EM was duplicated and performed with ab initio models generated from the data. No external data was input into the image processing. Current recordings from single channels were repeated on four different cells. Only cells with leak currents below 10 pA and with low electrical noise were recorded for temperature dependence. All successful electrophysiological recordings were reproducible.
Randomization	These experiment were not randomized. Covariates were minimized by comparing different conditions on the same experimental day to minimize batch effects.
Blinding	The investigators were not blinded to the data analysis. This is not technically or practically feasible for Cryo-EM and patch clamp. Researchers conducting the data analysis for each experiment were also responsible for data collection, making blinding impossible.

Reporting for specific materials, systems and methods

We require information from authors about some types of materials, experimental systems and methods used in many studies. Here, indicate whether each material, system or method listed is relevant to your study. If you are not sure if a list item applies to your research, read the appropriate section before selecting a response.

Materials & experimental systems

n/a	Involved in the study
☒	☐ Antibodies
☐	☒ Eukaryotic cell lines
☒	☐ Palaeontology and archaeology
☒	☐ Animals and other organisms
☒	☐ Clinical data
☒	☐ Dual use research of concern
☒	☐ Plants

Methods

n/a	Involved in the study
☒	☐ ChIP-seq
☒	☐ Flow cytometry
☒	☐ MRI-based neuroimaging

Eukaryotic cell lines

Policy information about cell lines and Sex and Gender in Research

Cell line source(s)	HEK293T (ATCC, CRL-3216) for electrophysiology. Expi5f9 Cells (Gibco, A35243) for baculovirus production. Expi293F GnTI- cells (Gibco, A39240) for protein production.
Authentication	Cells are routinely used in our labs and were not specifically validated for these studies outside of the manufacturer's specifications.
Mycoplasma contamination	Cell lines tested negative for mycoplasma.
Commonly misidentified lines (See ICLAC register)	No commonly misidentified lines were used for this study.

Plants

Seed stocks	N/A
Novel plant genotypes	N/A
Authentication	N/A